Annemarie Nadort, Jiangbo Zhao and Ewa M. Goldys
Lanthanide upconversion luminescence at the nanoscale: fundamentals and optical properties
Nanoscale, 2016; 8(27):13099-13130

Published at: http://dx.doi.org/10.1039/c5nr08477f

Lanthanide upconversion luminescence at a nanoscale: fundamentals and optical properties

Annemarie Nadort[a], Jiangbo Zhao[b] and Ewa M. Goldys[a]*

[a]*ARC Centre of Excellence for Nanoscale BioPhotonics, Macquarie University, Sydney 2109, NSW Australia*

[b]*ARC Centre of Excellence for Nanoscale BioPhotonics, Institute for Photonics and Advanced Sensing, School of Physical Sciences, The University of Adelaide, Adelaide 5005, SA Australia*

E-mail: ewa.goldys@mq.edu.au

Abstract

Upconversion photoluminescence is a nonlinear effect where multiple lower energy excitation photons produce higher energy emission photons. This fundamentally interesting process has many applications in biomedical imaging, light source and display technology, and solar energy harvesting. In this review we discuss the underlying physical principles and their modelling using rate equations. We discuss how the understanding of photophysical processes enabled strategic influence over the optical properties of upconversion especially in rationally designed materials. We subsequently present an overview of recent experimental strategies to control and optimize the optical properties of upconversion nanoparticles, focussing on their emission spectral properties and brightness.

TOC

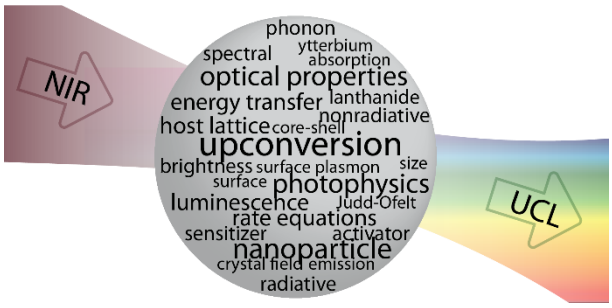

Abbreviations

UC - upconversion
UCL - upconversion luminescence
Ln or Ln^{3+} - lanthanide ion
UCNP – upconversion nanoparticle
ETU – energy transfer upconversion
GSA – ground state absorption
ESA – excited state absorption
ET – energy transfer
EM – energy migration
A – activator
S – sensitizer
ED – electric dipole
MD – magnetic dipole
DOS – density of states
PAT – phonon-assisted energy transfer
UV – ultraviolet
VIS - visible
NIR – near infrared
FRET - fluorescence resonance energy transfer
CE - conversion efficiency
QY - quantum yield
P_{em} - emitted power
P_{abs} - absorbed power
I_{ex} - excitation intensity
E_{ph} - photon energy

Contents

1. Introduction

The process of upconversion (UC) has been discovered in solid state materials in the 1960s and for a long time it has remained a scientific curiosity, as a very weak effect with limited practical applications[1-3]. Later, with the introduction of solid state lasers it gained increased visibility as a parasitic process competing with laser action on the one hand[4], or indeed it can provide the basis

of an efficient nonlinear laser excitation scheme[5, 6]. Since the mid-1970s first reports of efficient upconversion in co-doped materials have started to appear which led to renewed interest in this field[7-9]. The interest in this field intensified further when high brightness upconversion has been reported in nanomaterials[10, 11], as they can be produced more cheaply than thin films or crystals. This was followed by the realisation that upconverting nanomaterials lend themselves to a variety of applications across many fields recently summarised by Zhou *et al.*[12]. A significant amount of work has now been published on various aspects of upconverting nanomaterials, and we refer the reader to a number of excellent reviews, including on advances in the synthesis and chemistry of upconversion nanoparticles (UCNPs)[13, 14], the application of UCNPs to theranostics[15] and drug delivery[16], and theoretical advances in the understanding of upconversion in nanomaterials[17]. We highlight a recent review by Liu *et al.*[18] focused on measurement techniques for UCNPs, and their physical and optical parameters. Much of the published work centres around nanomaterials chemistry, where successes are often achieved by trial and error. Further progress can be made by more detailed understanding of these materials, currently far from complete. Therefore we feel that this field will benefit from wider understanding of physical principles of UC which may inspire a more rational materials design. To this aim we discuss here photophysics of upconversion, with aspects such as the influence of defect density on UCL, establishing the key upconversion mechanisms in the rate equations, and the limitations of the rate equations being reviewed for the first time. The photophysical processes are, generally, common to bulk materials (bulk crystal and thin films), nanoparticles and molecular clusters; however some of their aspects subtly differ. In particular, nanomaterials and molecular clusters are significantly more affected by the processes occurring on and near the surface (such as for example ligand and solvent quenching), while bulk materials and nanomaterials benefit from the opportunities afforded by the scaffolding of the crystalline lattice such as the ability to introduce secondary ions actively participating in the upconversion process. Molecular upconverting systems do not currently utilise this option[19].

The process of upconversion luminescence (UCL) involves excitation of a material (solid state material or a molecular system) with lower energy photons which stimulates the emission of higher energy photons. The process must satisfy the energy conservation principle, and, to ensure that, each higher energy emission photon requires two or more lower energy excitation photons. The UCL mechanism is distinctly different from other optical processes which also use two or more lower energy photons to yield higher energy emissions, such as multiphoton (most frequently two-photon) fluorescence and second (third, fourth etc) harmonic generation[20-22]. The key distinction is the involvement of intermediate electronic states in the upconverting system. The process of UCL is mediated by real electronic states, while in multiphoton fluorescence and second (third, etc) harmonic generation, such real intermediate electronic states do not take part. Due to this difference, the two-photon fluorescence and second harmonic generation based on simultaneous interaction of two or more photons require 5–10 orders of magnitude higher excitation powers but yield more than 5 orders of magnitude lower quantum efficiency in comparison to UCL[20, 23-25].

The intermediate states involved in UC must be excited, and because of that, the process is most pronounced in material systems where these states have relatively long lifetimes. This is because a state with long lifetime is able to accumulate sufficient transient population, which increases the probability of interaction with subsequent photons. This condition is met by quantum systems with parity-forbidden, but partly allowed optical transitions, such as lanthanide (Ln) and transition metal ions and other heavier elements in the periodic table[26, 27]. Due to a high degree of shielding of the f and d orbitals in such ions, they retain their atomic-like emission characteristics even when placed in a crystalline matrix. These parity-forbidden transitions exhibit long lifetimes, often in the range of hundreds of microseconds to milliseconds. Ln-doped materials are most frequently investigated in the context of upconversion, and they have been attracting increased attention since the discovery of efficiently upconverting materials on a nanoscale[10, 11]. We note that Ln-doped materials have also proven useful as downconverting photoluminescent agents, and refer the reader to excellent reviews by Bünzli [28, 29].

This review is organised as follows. In Section 2 we present an overview of the principal parameters that influence upconversion, such as the luminescent centres and the host lattice materials, and we briefly discuss its core mechanisms, focusing on two-photon excitation. Section 3 discusses in-depth the photophysics of upconversion and explains the fundamental photophysical processes. Section 4 describes practical approaches to formulating rate equations and the establishment of mechanisms of relevance for UCL. Section 5 then describes how the knowledge of the UCL processes can be used to influence the optical properties of upconverting nanoparticles (UCNPs), by providing an overview of recent reports concerned with spectral emission properties (colour) and brightness of UCL. We conclude with a short outlook on future directions in the field of UCL.

2. Principal factors that influence upconversion

2.1 Luminescent centres

Many of the well-known UC materials use trivalent lanthanide (Ln^{3+}) ions as the luminescent centre, typically Er^{3+}, Tm^{3+}, Ho^{3+}, Pr^{3+}, Nd^{3+}, although transition metal and actinide ions are also capable of upconversion[30]. Ln^{3+} doped materials are particularly well suited for UCL because the f electrons in the inner shells of Ln^{3+} ions are well shielded from their chemical environment by the outer-lying s and p electrons, which are involved in the bonding with the host material. These strongly shielded f states are rather insensitive to the surrounding host lattice (i.e. the crystal field and, to a lesser extent, the site symmetry), resulting in weak electron–phonon coupling. As a consequence, the energy states of Ln^{3+} ions in varying lattices are similar to those in free Ln^{3+} ions, with sharp and well defined spectroscopic features (10~20 nm FWHM). Due to these f states, Ln^{3+} ions commonly have multiple spectroscopically active levels (with the exception of Yb^{3+} and Ce^{3+}) characterised by long lifetimes typically in the microseconds to millisecond range, and a large number of close energy levels, which can therefore facilitate multiple types of upconversion processes. The energy states of Ln^{3+} ions are specified in terms of spin (*S)*, orbital

(L) and total angular momentum (*J)* of each of their f electrons, and denoted in Russell–Saunders notation as $^{2S+1}L_J$ [31].

UCL frequently involves more than one type of a centre. The luminescent centre emitting UCL is always involved; this centre is referred to as an "activator". However, in 1966 Auzel reported on the much more efficient UCL process involving partner ions that harvest the light, followed by energy transfer to the activator[3, 32]. The light harvesting ions are referred to as "sensitizers". Sensitized upconversion is discussed in more details in the forthcoming sections.

2.2 Host lattice

The host lattice plays a significant role in enabling bright UCL. As a rule of thumb, the host lattice is required to be transparent to excitation light and upconversion emissions. Most crystalline lattices of relevance to UCL have bandgaps greater than ~6 eV, corresponding to the wavelength in the deep UV of 206 nm. These host materials are transparent to a range of f-f transitions that occur within its bandgap. To ensure high UCL efficiency the host lattice must provide asymmetrical crystal field, achieved when the site symmetry of the Ln^{3+} ion is low. This is because the f-f electric dipole (ED) transitions of a free Ln^{3+} are parity-forbidden. In an asymmetrical crystal field, the f states of Ln^{3+} ions are able to interact with other Ln^{3+} states of opposite parity, leading to mixed parity states between which the original parity-forbidden f-f electric dipole transitions become allowed[33]. In principle, a stronger asymmetric contribution from the crystal field increases the extent of opposite parity mixing, hence enhancing the optical transition probabilities (absorption and emission) in Ln^{3+} ions. The allowed magnetic dipole (MD) transitions are much less affected by the crystal field.

Varying the degree of crystal asymmetry of the host is one of leading methods to enhance the efficiency of UCL. This can be seen, for example when the site symmetry of the Er^{3+} ion is reduced from the most symmetric O_h symmetry in cubic $NaYF_4$ to C_{3h} in hexagonal $NaYF_4$, and from D_{4h} in tetragonal ZrO_2 to C_{2h} in monoclinic ZrO_2[10, 34-37]. In both cases, the Er^{3+} ion exhibit approximately 10 times brighter UCL in a lower symmetry host lattice. The host lattice not only has a significant effect in transition probabilities of Ln^{3+} ions by lower site symmetry but it also can influence the UCL wavelength by shifting the energy levels.

The f energy levels of Ln^{3+} are affected by a combination of Coulomb force, spin-orbit coupling, and the influence of the surrounding distributed charge including the crystal field which induce their splitting. The ^{2S+1}L splitting imposed by the electrostatic interaction is on the order of 10^4 cm^{-1}, while the spin-orbit coupling removes the degeneracy of states with the same J, with splitting of the order of 10^3 cm^{-1}. The crystal field strength is responsible for their further shifts, in the order of 10^2 cm^{-1} [38]. Therefore, the resulting energies of Ln^{3+} electron states are primarily determined by the site symmetry and crystal-field strength of the lattice. The energy shifts of Ln^{3+} emissions in various host materials can be quite significant[17, 39, 40]. Adjusting the energies of electronic states of the $^{2S+1}L_J$ multiplets through selecting and modulating the host lattice has therefore become one of the important methods to enhance and tune UCL.

Another key requirement for a host lattice suitable for efficient UCL is low phonon energies. The absence of high energy phonons reduces the effects of undesired nonradiative multiphonon relaxation (details are discussed in the following section). This enables the conversion of a higher ratio of excited photons into UC emission. The effect of phonon energy on the UCL efficiency may be more significant than the effect of low site symmetry of the Ln^{3+} ion in a crystalline lattice. For example, Ln^{3+} dopants in β-$NaYF_4$ (hexagonal phase $NaYF_{4)}$ occupy a crystalline site with a relatively high C_{3h} symmetry, while β-$NaYF_4$ is currently recognized as the most efficient host lattice for UCL[41]. This indicates that the site symmetry effect is more than compensated by the average low phonon energy.

2.3 Other parameters of significance

The recent surge or research interest in UCL has led to multiple sophisticated approaches to optimise its spectral properties and brightness. In Fig. 1a we present a schematic overview of the different routes to influence these properties. The spectral properties are affected by (a) the choice and combination of activators with available radiative transitions[42], or (b) by judiciously selecting the host matrix and designing optical properties around the emitters (see Sections 2.1 and 2.2). Other routes involve (c) the variation of concentration of Ln^{3+} ions[43, 44]; (d) changing the nanocrystal size[45, 46]; or (e) changing the excitation schemes in both excitation power density and excitation pulse duration[47, 48], all resulting in favouring certain radiative and nonradiative processes within the Ln^{3+} (co)-doped matrix, and eventually tuning the output colour. Finally, (f) external materials can also influence the UC spectral properties, this can be accomplished, for example, by coating the particles with absorbing or fluorescent dyes[49, 50]. The application of these routes for controlling the UCL spectral properties, individually, or in combinations, are described in Section 4.1. Similar approaches can be utilized to enhance the UCL brightness. For example, (a) optimizing the types and concentrations of Ln^{3+} ions can result in brighter particles, but equally important is (b) the composition and geometry of the host matrix: intuitively a high Ln^{3+} concentration would yield a higher UCL brightness, however, it was shown early on that high concentrations result in quenching of UCL[10]. This can be overcome by (c) separating the ions in core-shell structures[51], (d) clustering of sensitizers[52], or (e) using high excitation power density schemes[23, 25]. Finally, (f) external materials can be used to enhance the upconversion brightness, for example using metal substrates to induce surface plasmon resonance[53]. These approaches are described in more details in Section 4.2.

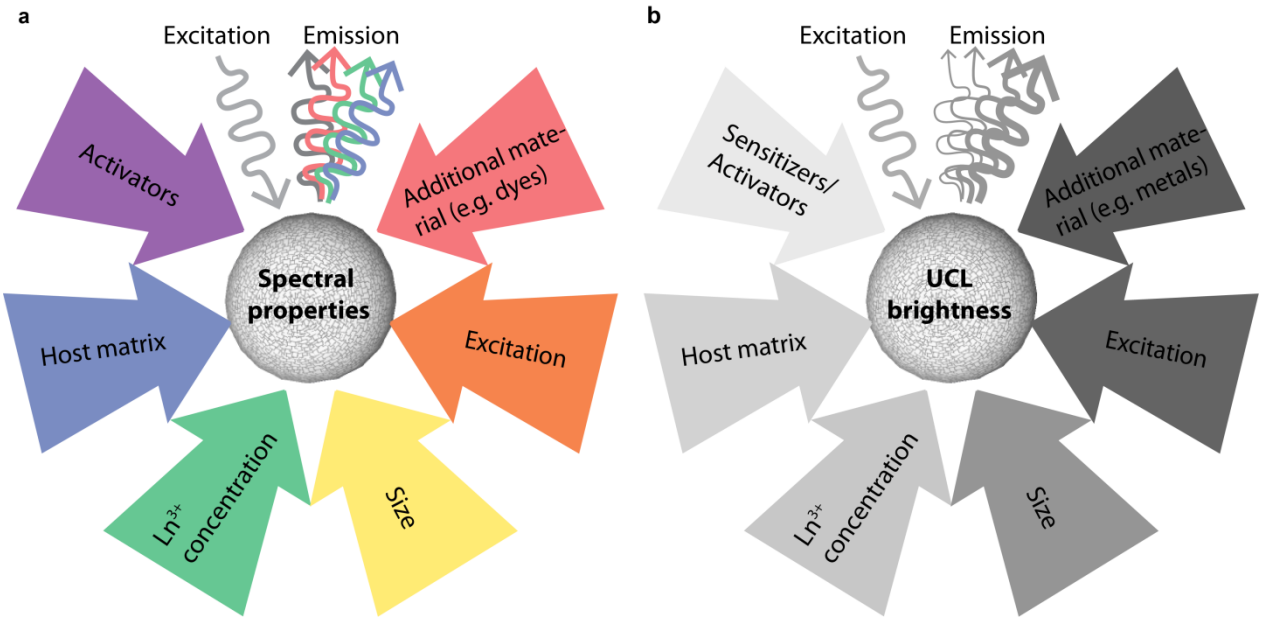

Fig. 1. Schematic diagram showing different avenues to influence the UCL spectral (a) and brightness (b) properties. More details are described in Sections 3 and 5.

3. Photophysics of upconversion

3.1 Upconversion mechanisms

The UC process can take place through a number of complex but remarkably efficient pathways. Indeed, it is the discovery of one of these complex pathways (energy transfer upconversion, ETU) has transformed the field of UCL[30]. The UCL involves several photophysical processes in the centre(s) involved: ground state absorption (GSA), and either excited state absorption (ESA), or energy transfer (ET), or both, and optional energy migration (EM) (Fig 2).

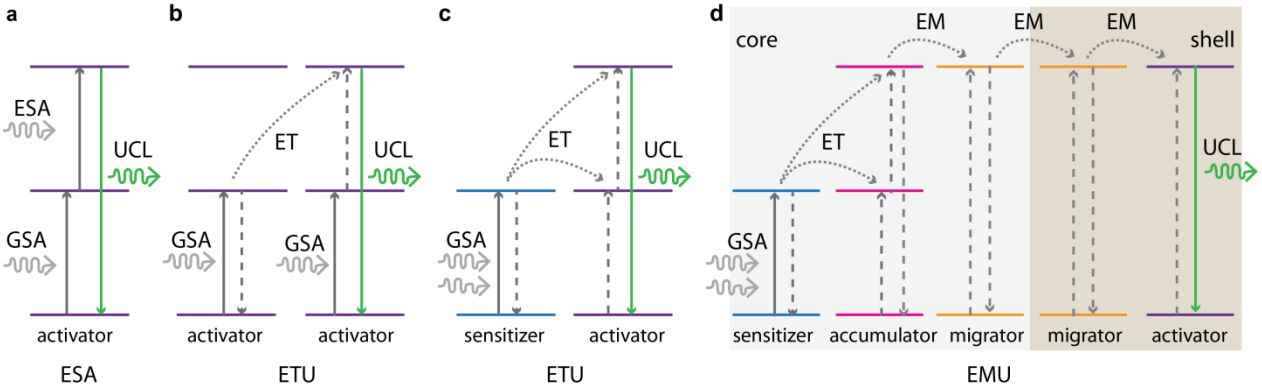

Fig. 2. Key mechanisms for UCL involve GSA, ESA and ET steps, resulting in (a) GSA/ESA, (b) GSA/ETU (activator-activator, AA), (c) GSA/ETU (sensitizer-activator, SA), and (d) EMU mechanism. As shown in (b) and (c), GSA/ETU can occur in the same type of ions (b), or two different ions (c). The EMU mechanism involves multiple types of ions and a core-shell design, as described in Ref [54].

The key upconversion mechanisms GSA/ESA, GSA/ETU, and GSA/EMU[30, 54, 55], illustrated in Fig. 2a-d combine these fundamental processes. GSA/ESA is the simplest single-centre UC mechanism in which two photons are sequentially absorbed by GSA in an ion responsible for UC called "activator". Subsequent to that an ESA takes place via a real intermediate energy level, and the same centre then emits UCL (Fig. 2a). The most frequently exploited GSA/ETU mechanism involves a second, auxiliary centre which is excited by GSA and then transfers its excitation energy by ET to the activator centre responsible for UCL. Simultaneously, the auxiliary centre relaxes to its ground level. There are two types of GSA/ETU mechanisms. One of them is the GSA/ETU which involves a pair of identical ions, an activator-activator pair (AA, Fig. 2b), where intermediate states of two identical centres are excited by GSA, followed by further excitation of one of the centres to a higher energy level via the ET. The alternative GSA/ETU mechanism (Fig 2c) involves two different centres - sensitizer-activator pair, SA. Here, a non-upconverting sensitizer ion absorbs the excitation photons by the GSA step and the activator centre which is sequentially excited to its intermediate and emitting energy levels emits the UC signal. Finally, the EMU is a derivative GSA/ETU mechanism combining GSA, ET, and EM steps, and it may involve up to four types of centres[54]. In the EMU mechanism, a sensitizer centre excited by GSA first transfers its excitation energy to an accumulator centre. The ideal sensitizer has a large absorption cross section, and energy levels closely matching the energy gaps of the accumulator's intermediate levels. The accumulator is required to have a long lifetime to consecutively accept and accumulate energy from the sensitizer. The EM then occurs from the high-lying excited state of the accumulator to a migrator centre, followed by migrating the excitation energy via the migrator ion through the core–shell interface. The ideal migrator has a long lifetime which decreases the decay rate of the excitation energy through optical transitions. The sensitizer/accumulator and the activator are spatially confined in different layers of the core–shell structure, bridged by arrays of energy transferring migrators, which reduces cross relaxation and ensuing luminescence quenching. Subsequently, the migrated energy is trapped by the activator centre in the shell which then emits the UCL. The migrator facilitates one-step energy transfer to the activator, significantly relaxing the requirements on the activator (such as long lifetime and intermediate energy levels). This recently introduced GSA/EMU mechanism[54] for the first time expands the UCL to Ln^{3+} ions where the intermediate states cannot be excited at 980 nm, such as Eu^{3+}, Tb^{3+}, and Sm^{3+}.

3.2 Photophysical processes

The key photophysical processes in UCL of Ln^{3+} ions discussed above include the absorption of excitation photons (possibly stepwise in the case of ESA), subsequent energy transfer processes, and finally the release of excitation energy, in particular radiative emission of the upconverted, high energy photons. Numerous competing radiative and nonradiative relaxation processes and phonon-assisted energy transfers may also be involved simultaneously. They all play a vital role to determine the luminescence efficiency and relative intensities of UCL at different wavelengths. Therefore, understanding of these key photophysical processes of UCL is essential for materials

design and optimisation, and it enables qualitative and quantitative interpretation of experimental data.

3.2.1 Photon absorption and emission – Judd-Ofelt theory

Absorption of the excitation photons by GSA initiates UCL. The theory of absorption and emission in quantum systems such as Ln^{3+} ions is well established[56, 57]. The emission intensities are related to quantum-mechanical transition rates between the energy levels involved[58]. These transition rates depend on the details of the initial and final states taking part in the emissions. In the case of Ln^{3+} ions, these initial and final states are two different $4f^N$ states with added components of opposite parity $4f^N5d$ states whose magnitude depends on the electric field strength of the surrounding crystal. The effects of the crystal field on the wavefunctions of free Ln^{3+} ions are not easily accessible experimentally.

In order to enable practical calculations of optical properties of Ln^{3+} ions in crystals, Judd and Ofelt introduced a simplified approach to the calculation of radiative rates in these ions embedded in a crystalline matrix. This approach is based on a number of approximations about energies of the component states. It assumes that all Stark levels in a manifold are equally populated and that the matrix elements are isotropic[59, 60]. These assumptions are reasonably well met by many specific lanthanide-matrix configurations. The Judd-Ofelt approach is important because it makes it possible to replace some parameters that are quite difficult to accurately estimate theoretically by experimental parameters easily obtained by fitting optical absorption or emission (line strength) data. This enables us to estimate radiative rates for the Ln^{3+} ion-matrix combinations with the aid of simple absorption or photoluminescence experiments[61].

In Judd-Ofelt approach, the radiative rate W_{rad} (in photons/sec) between two manifolds of a Ln^{3+} ion, the initial state $|SLJ\rangle$ and the final state $|S'L'J'\rangle$ for an electric dipole (ED)-allowed transition can be approximated by[57, 62-68]:

$$W_{rad} = \frac{4e^2\omega^3}{3\hbar c^3}\,\frac{1}{2J+1}\,n\left(\frac{n^2+2}{3}\right)^2 \sum_{\lambda=2,4,6}\Omega_\lambda\,|\langle SLJ\|U^{(\lambda)}\|S'L'J'\rangle|^2 \qquad (1)$$

Here, e is electron charge, ω is the average angular frequency of the optical transition, $\hbar$ is the reduced Planck constant, c is the speed of light, n is the refractive index and $[(n^2+2)/3]^2$ is the Lorentz local field correction factor, $2J+1$ is the degeneracy of the initial state. $|\langle SLJ||U^{(\lambda)}||S'L'J'\rangle|^2$ are the squared matrix elements of the ED operator between the initial and final manifolds, which depend on the angular momentum of the Ln^{3+} ion but are independent of the host matrix. These have been tabulated in the literature including in frequently cited works by Carnall[56] and Kaminskii[69]. The Ω_λ ($\lambda = 2,4,6$) are phenomenological parameters, known as Judd-Ofelt parameters. They capture the influence of the host matrix on the ED transition probabilities. The Judd-Ofelt parameters can be obtained by optical characterization of the material under investigation. This is because the quantity under the sum in Eqn. (1), $S_{ED}(J \rightarrow J')$ defined as:

$$S_{ED}(J \to J') = \sum_{\lambda=2,4,6} \Omega_\lambda \, |\langle SLJ \| U^{(\lambda)} \| S'L'J' \rangle|^2 \quad (2)$$

and known as the line strength between two states $|SLJ\rangle$, and $|S'L'J'\rangle$, is related to spectrally integrated absorption cross-sections for the relevant $J \to J'$ transitions:

$$S_{ED}(J \to J') = \frac{3ch(2J+1)}{8\pi^3 \bar{\lambda} e^2} n \left(\frac{3}{n^2+2}\right)^2 \int \sigma(\lambda) d\lambda \quad (3)$$

where *σ(λ)* is the absorption cross section as a function of wavelength. The line strengths, and consequently the Judd-Ofelt parameters can be derived from absorption measurements. The details of the fitting procedure are described in Ref.[70]. Judd-Ofelt parameters can also be obtained from the emission spectra (see Ref.[61] and references therein). The Judd-Ofelt theory with due consideration of the possible branching makes it possible to obtain radiative lifetimes of excited states.

We discussed here the ED transitions only, but we should add that both electric and magnetic dipole transitions can be observed in luminescence or absorption spectra of Ln^{3+} ions in a host matrix. The MD transitions are particularly pronounced in the infrared spectral range. These MD transitions are allowed between states with the same parity. The MD transitions in free ions are normally orders of magnitude weaker than ED transitions. However since the ED transitions for the Ln^{3+} ions are, in principle, forbidden and only partly allowed because of the perturbations caused by the host crystal, the spectral signatures of ED and MD transitions may be comparable in specific cases. MD transitions are only weakly affected by the crystal field and they can therefore be used as a benchmark for ED transitions described by the Judd-Ofelt formalism[61]. Alternatively, the relevant MD transition rates may be added to the Judd-Ofelt rates as in Ref. [71]. For completeness we add that the full quantum-mechanical theory of the optical transitions as well as the Judd-Ofelt approach is applicable to all optical transitions in the lanthanides including upconversion luminescence.

3.2.2 Resonant energy transfer

After absorbing the excitation photons, resonant energy transfer within the sensitizer-activator pair successively transfers the excitation energy of the sensitizer in an excited electronic state to a nearby activator centre either in its ground state or intermediate state. The energy transfer may be either non-radiative or radiative. The non-radiative resonant energy transfer is through long-range dipole-dipole interactions while the radiative resonant energy transfer requires emission and reabsorption of a photon. In this review, only the leading resonant non-radiative energy transfer is considered[30].

The energy transfer rate between the sensitizer and activator ions, W_{SA}, in the Förster-Dexter model[30, 72, 73], can be expressed using the spectral overlap of the sensitizer emission and activator absorption. The resonant energy transfer rate is given by:

$$W_{SA} = \frac{W_S}{R^6}\frac{3}{4\pi}\left(\frac{hc}{n}\right)^4 Q_A \int \frac{f_S^{ems}(E)\, f_A^{abs}(E)}{E^4} dE \quad (4)$$

where W_s is the radiative rate of the sensitizer ions in the absence of activators (equal to its reciprocal of the radiative lifetime, see Section 3.2.5), $\hbar$ is the reduced Plank's constant, c is the speed of light, n is the refractive index of the host lattice medium, Q_A is the integrated absorption cross section of the activator ion, and the integral expresses the spectral overlap of sensitizer ion emission and activator ion absorption, as a function of photon energy E ($E=hc/\lambda$).

Eqn. (4) can be rewritten in a simplified form:

$$W_{SA} = W_S \left(\frac{R_0}{R}\right)^6 \quad (5)$$

where R is the distance between the sensitizer and activator ion, and R_0 is known as the Förster radius. The Förster radius is, the distance at which the energy transfer rate W_{SA} is equal to W_S. Eqn. (5) indicates that W_{SA} is proportional to an inverse power of the distance R (as R^{-6}), and it rapidly decreases when $R>R_0$. In a random distribution of ions in the material, R may be taken as the average distance between the sensitizer and activator ions, Eqn. (5) then indicates that a sufficient ion density of sensitizers and activators is necessary for efficient energy transfer to produce bright UCL until the concentration quenching takes effect (as discussed below). In addition, the sensitizer ions with larger W_S are beneficial for more efficient energy transfer. The ET step (introduced in Section 3.1) can be described by a generalization of the Förster-Dexter energy transfer model of the case where the activator is in an excited state instead of ground state.

The average distance between the sensitizer and activator is a useful parameter for the evaluation of chosen dopant concentrations and a host lattice. As an example, we show here the calculation of a typical average distance of between Yb^{3+} -Er^{3+} in $NaYF_4$, one of most efficient upconversion host materials[74]. The Yb^{3+} and Er^{3+} can be used to substitute the host Y^{3+} ions without changing the crystal structure. The lattice mismatch between β-$NaYF_4$ and β-$NaErF_4$ is only 0.13% and 0.25% for the lattice parameters a and c, respectively, therefore differences in the lattice parameters resulting from the Yb^{3+} and Er^{3+} ions doping can be neglected[74]. β-$NaYF_4$ crystallizes in a space group $P\bar{6}$ and its unit cell corresponds to the structured cell formula β-$Na_{1.5}Ln_{1.5}F_6$. This means that there is Z= 1.5 Y^{3+} ions in each unit cell[75]. The respective lattice parameters for β-$NaYF_4$ are a = 5.9757 Å and c = 3.5305 Å (+/- 0.1%). The Ln^{3+} cation sites are considered to be disordered and randomly distributed. The average Yb−Er distance d can be approximated by the cubic root of the corresponding unit cell volume divided by Z and the Yb^{3+} and Er^{3+} doping percentages x and y over total Ln^{3+} cationic sites:

$$d_{\beta-NaYF_4} = \left(\frac{a^2 c\sqrt{3}/2}{1.5(x+y)}\right)^{1/3} \quad (6)$$

where *a* and *c* are the lattice parameters of the hexagonal unit cell with a volume of $a^2c\sqrt{3}/2$. According to Eqn. (6), for 20% Yb and 2% Er in $NaYF_4$, we can estimate the average Yb−Er distance to be around 6.5068 Å.

The sensitizer-activator pairs in a crystal have a varying distance determined by the lattice parameters. For each pair, the corresponding energy transfer rate W_{SA} varies as R^{-6}. The statistical analysis of W_{SA} at such varying distances has been considered by assuming a random spatial distribution of activator ions around a sensitizer in a crystal. The calculated average energy transfer rate $\langle W_{SA} \rangle$ is given by:[30, 76]

$$\langle W_{SA} \rangle = \int_{R_{min}}^{\infty} W_{SA}(R)\omega(R)dR \quad (7)$$

where $\omega(R)dR$ is the probability distribution function of the sensitizer-activator distance *R*. This function specifies the fraction of sensitizer ions having an activator ion in a shell between *R* and $R+dR$.

We should also note that when activators are present, the relaxation of the sensitizers occurs not only because of the energy transfer, but also due to a competing process of their spontaneous deactivation including light emission and nonradiative relaxation in the sensitizer. However, at the optimal doping concentration of activators, the relaxation rate of sensitizers is dominated by the energy transfer. Secondly, sensitizer ions are most likely present at high concentration, e.g., Yb^{3+} ions in the range of 20~40%. This facilitates high energy diffusion rate between sensitizers which may be faster than their own spontaneous decay rate and sensitizer-activator energy transfer rate. In these conditions, Eqn. (7) can be simplified as[30, 77]:

$$\langle W_{SA} \rangle \cong \langle W_S^* \rangle = CN_A \quad (8)$$

where $\langle W_S^* \rangle$ is the statistical averaging of relaxation rate of sensitizers codoped with activators, *C* is the excitation migration constant ($cm^3\ sec^{-1}$) associated with the average distance activator-sensitizer distance, and N_A is the activator concentration. As a result, the energy transfer rate is linearly dependent with the activator concentration. This agrees well with experimental observations at low activator concentrations[30, 77]. However, the UCL intensity reaches an optimum with increasing ion concentration, after which the UCL intensity decreases with further increasing ion concentration. This concentration quenching effect, which over-compensates the increased transfer rate at high doping levels, imposes a significant constraint to generate bright UCNPs. The mechanism leading to concentration quenching will be discussed in Section 3.2.5.

Finally we comment that any model of energy transfer established for bulk materials have to be modified in nanocrystals because of the reduction of phonon density of states (DOS) and limited number of sensitizers and activators in a nanoscale system, which can decrease the energy transfer rate. For example, there is a 14% decrease of the energy transfer rate in a 10 nm UCNPs compared with the bulk counterpart[17]. The effects of size in the DOS are well understood as

discussed from a theoretical perspective in Ref.[78]. Briefly, the overall DOS dramatically decreases in a nanoscale system. The integral of the phonon density of states over frequency is equal to the total number of phonon modes, $3N\text{-}6$, where N is the number of atoms in the nanoparticle. This decrease has a significant impact on all processes where the probability of interaction with a phonon is involved, such as multiphonon recombination and phonon-assisted energy transfer whose probabilities decrease with nanoparticle size. As a result of the reduced DOS with nanoparticle size, the relevant rates should decrease as well[79-81]. Moreover, in nanocrystals, the phonons being confined no longer have well-defined wave vectors, leading to the relaxation of the selection rules. Simultaneously, the overall electron-phonon coupling strength in nanocrystals decreases monotonically with increasing size[82]. The maximum phonon energy is determined by the interatomic spacing and is independent of nanoparticle size. However many low frequency phonons that exist in solids are no longer supported in nanoparticles, so the DOS is slightly rebalanced[82].

3.2.3 Phonon-assisted non-resonant energy transfer

The resonant energy transfer between sensitizer and activator considered by Förster requires identical energy gaps for the involved ions, as shown in Fig. 3a. However, frequently there is an energy mismatch between the energy levels of the sensitizer and activator ions, illustrated in Fig. 3b. It has been experimentally found that the energy transfer can still take place even the energy mismatch between Ln^{3+} ions as high as of the order of 10^3 cm^{-1}, (such as the 1600 cm^{-1} energy gap between $^2F_{5/2}$ Yb state and $^3H_5$ Tm state[83]) . The energy transfer in this case is facilitated by the nonradiative, phonon-assisted processes, where the energy mismatch is compensated by simultaneous emission or absorption of one or more phonons by the host lattice.

The phonon-assisted energy transfer (PAT) plays an especially important role in UCL when many stepwise energy transfers have an energy mismatch. The Equations (4) and (5) are still applicable to assess the energy transfer rate W_{SA}, but phonon sidebands must be included in the modified relationship. According to the Miyakawa-Dexter theory[84, 85], the probability of multiphonon-assisted energy transfer $W_{PAT}(\Delta E)$ is given by:

$$W_{PAT}(\Delta E) = W_{PAT}(0)e^{-\beta \Delta E} \quad (9)$$

where ΔE is the energy gap (mismatch) between the levels of sensitizer and activator ions, $W_{PAT}(0)$ is the energy transfer rate without energy gap, and β is a parameter determined by the strength of electron-lattice coupling as well as the nature of the phonon involved.

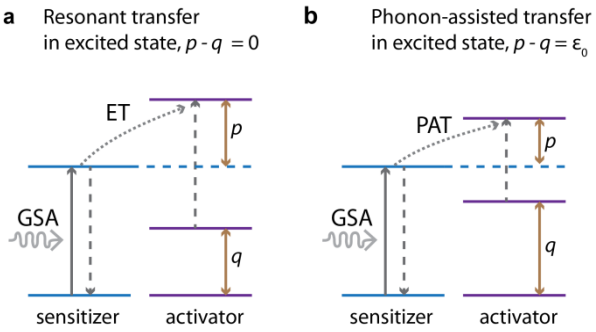

Fig. 3. Energy transfer (ET) from a sensitizer to an activator ion in an excited state. Non-radiative energy transfer can be resonant, with no energy mismatch (a); or phonon-assisted (PAT), with energy mismatch (b).

3.2.5 Nonradiative relaxation

The total radiative lifetime of a transition is the inverse of the relevant radiative rate, $\tau_{rad} = (W_{rad})^{-1}$. This rate can be estimated from the Judd-Ofelt analysis with or without the addition of MD transitions, and with due consideration of branching ratios. If a state can decay radiatively to several different final states with different values of J, the total radiative decay rate for the population of this state, W_{rad}, is obtained by adding their respective radiative rates. The total depopulation rate of this state, W_{tot}, is the sum of total radiative W_{rad} and total nonradiative rate W_{nrad}:

$$W_{tot} = W_{rad} + W_{nrad} \quad (10)$$

This total depopulation rate is the inverse of the observed luminescence decay lifetime τ, $W_{tot} = (\tau)^{-1}$. Eqn. (10) highlights that during the course of the excitation energy returning to lower energy states, the nonradiative relaxation in a luminescent system always competes with radiative transitions. Therefore, generally, the suppression of nonradiative relaxation is one of most straightforward methods to increase the upconversion brightness. Only in some specific cases nonradiative relaxation may be desired, by facilitating the energy transfer which cannot be realized by the phonon-assisted energy transfer and in tuning the optical properties of UCNPs, e.g., relative intensity for colour and lifetime for multiplexing. These applications will be illustrated and discussed in Section 5.

Among many nonradiative relaxation channels of an excited Ln^{3+} ion, multiphonon relaxation has a special place due to the shielding of f electrons in Ln^{3+} ions[77]. Miyakawa and Dexter developed a unified theoretical treatment to various multiphonon processes in the adiabatic approximation[85]. In this approach the multiphonon-assisted relaxation rate, W_{PAR}, is expressed in same form as in Eqn. (9):

$$W_{PAR}(\Delta E) = W_{PAR}(0)e^{-\alpha\Delta E} \quad (11)$$

where ΔE is the energy difference between the relevant levels occurring phonons relaxation in the luminescent system, $W_{PAR}(0)$ is a constant, and α is a host-specific parameter. Multiphonon relaxation is significant in perfectly crystalline materials; however real materials are frequently

contain high density of lattice defects, many of which may significantly contribute to nonradiative energy decays. This occurs via a two-step process: first the excited Ln^{3+} ion transfers its energy to a nearby defect centre. Subsequent to that the excited defect undergoes nonradiative relaxation. In particular, for small size nanoparticles where the near-surface region with higher defect density comprises most of the nanoparticle volume, these defect processes may dominate nonradiative relaxation. This effect underpins the well-documented size dependence of the observed UC luminescence lifetimes[46]. There is limited literature on specific effect of defects in nanoparticles due to characterization challenges[86, 87]. We were first to analyze the X-ray diffraction data in UCNPs to obtain information on defect densities[46].The XRD peak position is sensitive to the variation of the lattice constant due to defect induced strain, which provides a measure of the overall defect density. The XRD peak width depends on three major contributions, being crystallite size, instrumental broadening and defect density. In our previous work[46] measurement of the XRD peak width after correction for nanocrystallite size showed an increase of defect density with decreasing nanocrystal size. These crystalline defects provide the channels for nonradiative recombination[88], leading to a reduced lifetime as per the Stern-Volmer model[89].

Cross-relaxation is another nonradiative relaxation process of core significance in UCL. As shown in Fig. 4, in cross-relaxation, activator 1 is depopulated to a lower-energy level while activator 2 is populated to a higher-energy level, though not necessarily from the ground state. Obviously, cross-relaxation is a reverse of the upconversion process regarding the energy transfer step. Therefore, the concepts that explain resonance energy transfer can be generalised to describe cross-relaxation: the rate of cross-relaxation increases when two ions are in close proximity to each other. The cross-relaxation rates are related to the concentration of the relevant centres[30, 77, 90]:

$$\langle W_{CR} \rangle \cong C_M N_A \quad \text{(for ions with fast energy diffusion)} \qquad (12)$$

$$\langle W_{CR} \rangle \cong C_M N_A^2 \quad \text{(for ions with limited rate of energy diffusion)} \qquad (13)$$

where C_M is the excitation migration constant which depends on the average ion distance, and N_A is the activator concentration, respectively.

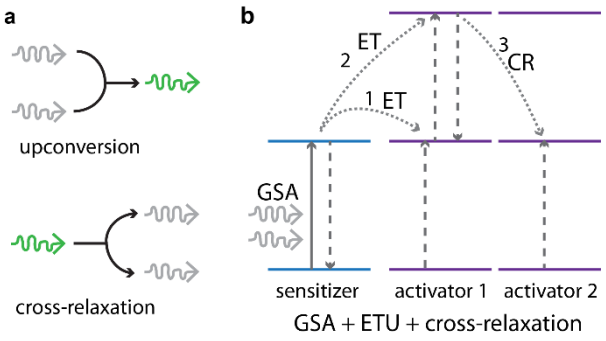

Fig. 4. (a) Schematic illustration of the energy transfer (ET) in upconversion and cross-relaxation (CR) processes and energy level diagram (b) of the ETU process followed by deleterious cross-relaxation, quenching the radiative energy level of activator 1.

For a dipole-dipole interaction, the overall upconversion rate of an excited Ln^{3+} activator ion after spatial averaging is reduced by the cross relaxation rate ($-\langle W_{CR}\rangle$). Owing to the excited ion population dependence of $-\langle W_{CR}\rangle$, the resulting UCL can only increase with activator concentration at low concentrations. Upon increasing the activator concentration, cross-relaxation becomes more pronounced, eventually leading to UCL decrease when it exceeds the optimal concentration threshold. This phenomenon is called concentration quenching, also well-known from the studies of fluorescence[91-93].

3.2.5 Competing luminescence processes

Among various processes that compete for excitation energy with the upconversion is conventional "downconversion" luminescence, as a range of $Ln3^{+}$ ions have optical transitions at energies lower than the excitation energy of the upconversion. A classic example is the Er^{3+} ion, with a 1.54 μm transition commonly utilized in the optical fibre technology[94], and similar infrared (IR) transitions in the Yb^{3+} ions[30] which reduce the excitation energy available to sensitize activators. There is also a possibility of downstream processes where excited higher energy levels responsible for the UC emissions decay via decay channels involving lower energy luminescence. The challenge of enhancing the UCL by reducing the downconversion emissions is compounded by the fact that they are both enhanced by making optical transitions more strongly allowed (by the influence of site asymmetry). This was demonstrated by the simultaneous enhancement of upconversion and downconversion luminescence at the same 980nm excitation in Al_2O_3 doped with Er, Yb:Er and Yb:Zn:Er, reported in Ref. [95]. We are not aware of engineering approaches to simultaneously enhance UCL and decrease the downconversion luminescence, while the excitation is at the same wavelength (e.g. 980 nm). Current efforts to optimize downconversion luminescence and UCL in the same material focus on applications in solar cells, where excitation energies for both luminescence processes are different and the enhancement of both is desired, as illustrated in [95-97]. There have been various efforts to analyse downconversion luminescence in Ln^{3+} ions[98].

3.2.6 Ligand/solvent quenching

The luminescence intensity in nanoparticles is quenched by solvent and/or ligands conjugated to the surface of nanoparticles. Ligand quenching occurs by any of the chemical ligands, but those comprising light elements whose vibrational energy is higher (such as -OH or –CH groups) quench nanoparticle luminescence more effectively. This is quantified by the generalized "gap rule", which relates the "gap" between initial and final energy level to the nonradiative rate and vibrational energy: $W_{nrad} \propto e^{-\alpha \Delta E/\hbar\omega}$ (see also Eqn. (11) and $\hbar\omega$ is the maximal vibrational energy)[46]. The vibrating bonds may be inside of the nanoparticle or immediately adjacent to it. As long as the vibrations are able to interact directly with the electronic excitations they will be able to dissipate energy. The degree of quenching by a specific ligand depends on the abundance of these ligands on the surface. The vibrating bonds do not have to be chemically attached to the nanoparticle surface, frequent collisions of molecules in the solvent with nanoparticle surface

provide enough opportunity for the excitation energy to be transferred to the vibrations of solvent molecules.

4. Rate equations

Experimental measurements of luminescence intensity and luminescence decay times are generally acquired from populations of luminescent ions. Thus, in order to link these observations to theoretical models, the models need to describe the behaviour of these populations. The rate equation approach centres on population behaviour and, although simplified, it enables quantitative predictions, as long as the required multiple parameters are known with sufficient accuracy. In the rate equations approach[23, 25, 46, 71, 100], individual energy transfers and other processes are represented by their population averages. This is a fairly coarse approximation for upconversion which generally requires a more nuanced and detailed understanding of random walks of excitation energy through the entire sensitizer-activator system. The physically most clear and intuitive understanding of upconversion in such systems is provided by a Markovian model which relates the rate of change of the probability that a single Ln^{3+} ion site is excited to the various microscopic molecular transfer probabilities[101-104]. This stochastic approach considers the interactions in the Ln^{3+} system of N ions as a random-walk process where occupation probabilities execute a hopping motion across the different ionic sites. However, such random walks are currently impossible to describe analytically and they have been addressed through numerical simulations only. Very few experimental works published so far have actively engineered these random walks, with notable exception of smart clustering approaches presented by Liu's group[52].

When setting up the rate equation model to analytically evaluate the UCL, the authors include mechanisms they regard to be of key relevance in the examined the system. Thus in each case specific assumptions and simplifications have been made, but without losing sight of core distinctions of interest in a particular problem. This is why different references show subtly different rate equations even in the same material system[23, 25]. Well-designed rate equations can give us valuable insights into microscopic processes in materials. For example, by experimentally measuring the decay rate W_{tot} and calculating the W_{rad} from the fundamental quantum-mechanical Judd-Ofelt analysis we can obtain W_{nrad} (Eqn. (10) and Section 3.2.1). While radiative rates of the Ln^{3+} ions are determined by the properties of the Ln^{3+} ions themselves and the matrix, the nonradiative rate depends on the choice of matrix and its phonons as well as by synthesis conditions which determine the defect density and conjugated ligands. They both critically affect not just observed decay times but also the overall brightness, as shown in the following simple analysis.

4.1. Basic rate equation

As an example, we show a basic rate equation describing luminescence in a three-level model of the ion with the aim to show how luminescence intensity is affected by the nonradiative relaxation. In this model the pump light, at the energy matching the energy difference between

the ground state 0 and the highest state 2, excites the electrons. We assume that they immediately relax to the level 1 (with an infinite rate) and these electrons, now on level 1 further decay to level 0 emitting luminescence, see the schematic drawing in Fig. 5a.

The basic equation for the transition rate between levels 1 and 0 at low excitation ($N_0 >> N_1$, where N_0 is the number of ions in ground state, N_1 is the population of ions in the first excited state) is:

$$\frac{dN_1}{dt} = AN_0 - N_1 W_{tot} = AN_0 - \frac{N_1}{\tau} \quad (14)$$

Here, dN_1/dt is the net transition rate from level 1 to level 0, τ is the decay constant (of radiative and nonradiative processes combined), and AN_0 is the absorption rate of the excitation photons between levels 0 and 2, W_{tot} is defined in Eqn. (10). In steady state conditions where $dN_1/dt = 0$, this becomes

$$N_1 = AN_0\,\tau \quad (15)$$

The photon emission rate from the emitting level 1 and using Eqn. (10) is then:

$$\frac{N_1}{\tau_{rad}} = AN_0 \frac{\tau}{\tau_{rad}} = AN_0 \left(\frac{W_{rad}}{W_{rad}+W_{nrad}}\right) \quad (16)$$

The emitted luminescence intensity, I [in Watts], related to the transition from initial level *1* to final level *0*, is given by [61]:

$$I_{10} = \hbar\omega_{10} W_{rad} N_1 \quad (17)$$

where $\hbar\omega_{10}$ is the transition energy between the levels 0 and 1.

Thus, in this basic model the luminescence intensity can be increased by increasing the activator doping (if no other processes are present) and the reduction of the nonradiative relaxation rate.

Below we show examples of how to set up rate equation models in more complex situations. The first case involves a minimal set of rate equations to model red and green UCL in a well-established upconverting Er:Yb system[46]. This model has been developed following Refs.[105, 106].

4.2. Example of rate equations describing red and green UC in an Yb-Er system

The relevant Yb^{3+} and Er^{3+}states are shown in Fig. 5b. We note that in this system the ground state is denoted '1', the first excited state '2', *etc*. These simplified rate equations describe the evolution of populations in the Yb^{3+} excited state (Yb_2) and four Er^{3+} states (Er_2), (Er_3), (Er_5), and (Er_6). $N_{Er(Yb),i}$ is the population density of the occupied level i of Er(Yb), and N_{Er} is the total density of Er^{3+} ions. We assumed that the Er^{3+} states above (Er_6) relax very rapidly to the state (Er_6) by multiphonon relaxation due to the small energy gaps, and the same argument applies to the state (Er_4), thus these were ignored in the rate equations. Our rate equations involve single-ion and two-ion processes only. The first single ion mechanism accounts for decay processes occurring within Er^{3+}starting from level i (i = 2, 3, 5, 6).

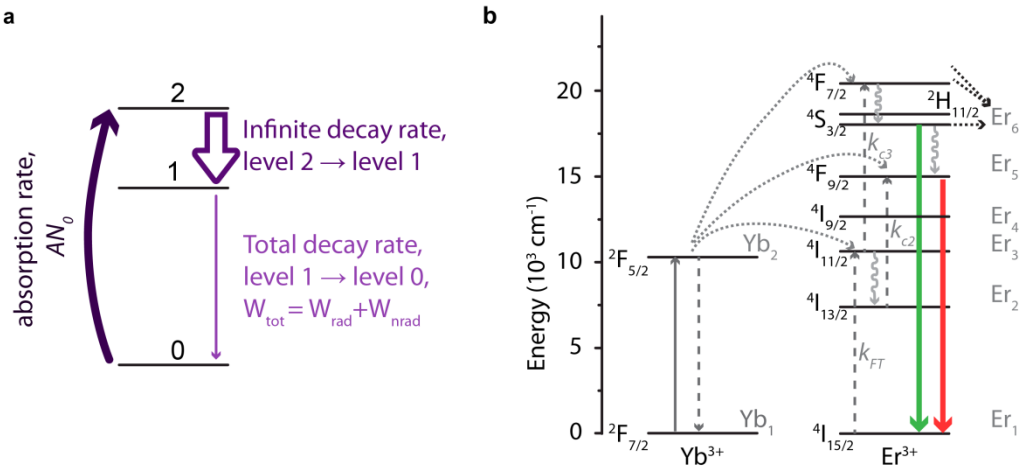

Fig. 5. (a) Schematic representation of simple 3-level model described in Section 4.1. (b) Main radiative and nonradiative transistions and energy transfer processes relevant for UCL in a $NaYF_4$:Yb,Er nanocrystal, described in section 4.2. The energy levels relevant in the rate equations are denoted $Yb_{1,2}$ and $Er_{1\text{-}6}$. Reproduced from Zhao *et al.*[46] with permission from The Royal Society of Chemistry.

W_{ij} describes the rate of population transfer of population from the *i*-th level to the *j*-th level ($i > j$). We also include single-ion processes within Yb^{3+} such as ground state absorption (GSA) and excited state absorption in Er^{3+} (ESA) described by the absorption cross sections σ_{Yb} for the ground state of Yb^{3+} and $\sigma_{ESA2(3)}$ for levels 2 and 3 in Er^{3+}. The latter process produces upconversion via ESA. Among the two-ion process, we only consider those that involve pairs of Yb^{3+}–Er^{3+} (cooperative upconversion via energy transfer upconversion (ETU)), and neglect the pairwise Er–Er energy transfer (cumulative upconversion). This is because Yb^{3+} sensitisation is well-known to be critical for strong upconversion emission in Er^{3+} doped nanocrystals at low excitation density[30]. We define $k_{c2(3)}$ as the cooperative upconversion coefficient for the 2->5 and 3->6 upconversion processes, respectively. k_{FT} is the coefficient of forward energy transfer Yb^{3+}/Er^{3+}, the main pathway for exciting Er^{3+}. However, we ignore the decay of Yb^{3+} by other channels than forward energy transfer to Er^{3+} because it is comparatively weak[107]. Back energy transfer from Er^{3+} to Yb^{3+} is ignored as well[107, 108], and radiative and non-radiative decay from Er^{3+} level 2 is considered to be negligible[109, 110]. With these conditions, the rate equations are formulated as[46]:

$$\frac{dN_{Yb,2}}{dt} = \rho_p \sigma_{Yb} N_{Yb} - k_{FT} N_{Er,1} N_{Yb,2} - k_{c2} N_{Er,2} N_{Yb,2} - k_{c3} N_{Er,3} N_{Yb,2} \quad (18)$$

$$\frac{dN_{Er,2}}{dt} = -k_{c2} N_{Er,2} N_{Yb,2} - \rho_p \sigma_{ESA2} N_{Er,2} - W_2 N_{Er,2} + W_{32} N_{Er,3} + W_{52} N_{Er,5} + W_{62} N_{Er,6} \quad (19)$$

$$\frac{dN_{Er,3}}{dt} = k_{FT} N_{Er,1} N_{Yb,2} - \rho_p \sigma_{ESA3} N_{Er3} - k_{c3} N_{Er,3} N_{Yb,2} - W_3 N_{Er,3} + W_{53} N_{Er,5} + W_{63} N_{Er,6} \quad (20)$$

$$\frac{dN_{Er,5}}{dt} = k_{c2} N_{Er,2} N_{Yb,2} + \rho_p \sigma_{ESA2} N_{Er,2} - W_5 N_{Er,5} + W_{65} N_{Er,6} \quad (21)$$

$$\frac{dN_{Er,6}}{dt} = k_{c3}N_{Er,3}N_{Yb,2} + \rho_p\,\sigma_{ESA3}N_{Er,3} - W_6N_{Er,6} \quad (22)$$

The symbol ρ_p denotes the excitation power variable, given by

$$\rho_p = \frac{\lambda_p}{hc\pi w_p^2}P \quad (23)$$

Here, P is the incident pump power, $\lambda_p$and $w_p$are the pump wavelength and beam radius, respectively, h is Planck's constant and c is the speed of light.

4.3. Example of rate equations to describe concentration quenching

The second example is a similarly minimal set of rate equations with the smallest number of energy levels able to describe UCL in the ETU mechanism, in the presence of concentration quenching[25, 45]. This concentration quenching was not included in the previous model. In our simplified approach the Ln^{3+} ion (activator) is represented by three states, L_{n0} , L_{n1}, and L_{n2}, with the same energy spacing between adjacent states, see Fig. 6a. The Ln^{3+} ions are excited by the sensitizer, Yb^{3+}. This requires the excitation of Yb^{3+} (GSA) between two energy states $Yb_{,0}$ and $Yb_{,1}$. The reverse energy transfer from Ln^{3+} back to Yb^{3+} is ignored, consistent with the situation in the Yb^{3+} - Er^{3+} system[107, 108], and the Ln^{3+} - Ln^{3+} cross-relaxation is taken into account. We also ignore radiative and nonradiative recombination within Yb^{3+}. The key energy transfer processes are illustrated in Fig. 6b.

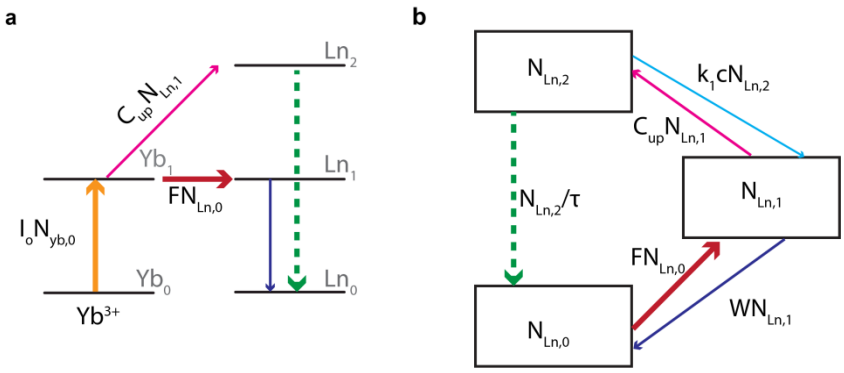

Fig. 6. (a) Energy spacing and energy transfer between different states of sensitizer Yb and the activator Ln-ion. (b) Schematic diagram of the key energy transfer processes represented in the rate equations (24)-(27). Rectangles represent state populations. Reproduced with permission from Zhao et al.[25], copyright 2013, Nature Publishing Group.

The rate equations for the excited state populations of the Yb^{3+} and Ln^{3+} ions are as follows:

$$dN_{Yb1}/_{dt} = AI_0\,N_{Yb,0} - FN_{Ln,0} - C_{up}N_{Ln,1} \quad (24)$$

$$dN_{Ln2}/_{dt} = -k_1cN_{Ln,2} - \frac{N_{Ln,2}}{\tau} + C_{up}N_{Ln,1} \quad (25)$$

$$dN_{Ln1}/_{dt} = k_1cN_{Ln2} - WN_{Ln,1} - C_{up}N_{Ln,1} + FN_{Ln,0} \quad (26)$$

$$dN_{Ln0}/_{dt} = \frac{N_{Ln,2}}{\tau} + WN_{Ln,1} - FN_{Ln,0} \quad (27)$$

Here $F = N_{Yb1} r_{FET}$ where r_{FET} is the forward energy transfer rate from Yb^{3+} to Ln^{3+}, and $C_{up} = k_{C,up} N_{Yb,1}$ is related to the upconversion process involving excited Yb^{3+} and Ln^{3+} in its first excited state, c is the concentration of Ln ions which have their first excited state empty, and k_1 is the decay rate between the second and first excited state of the Ln ion. AI_0 is a product of the excitation power variable and absorption cross section, $AI_0 = \rho_p \sigma_0$. The power constant is defined above, Eqn. (23).

We comment that the latter two models presented here (Eqns 18-27) describe the case of excitation which is high enough to ensure that the excited ion distribution is spatially homogeneous. In this case, by suitable statistical averaging over the distribution of the Ln^{3+} ions, the excitation probabilities can be integrated within a set of differential equations with macroscopic rate constants describing the populations on various excited states.

We also emphasise that the rate equation approach generally assumes that each of the included processes can be adequately represented by its average over the relevant population(s). Strictly speaking, this is not applicable to energy transfer processes because due to the short range of the energy transfer in the Forster formalism compared to the lattice constant, effective energy transfer may occur only between near or even nearest neighbours. However this does not affect the structure of the appropriate terms in the rate equation, as long as each specific energy transfer rate is characterised by a different constant.

Once the rate equations have been formulated one can consider various excitation regimes, by appropriately setting the excitation power variable. For example with a pulsed excitation we can explore the behaviour of populations of various states and UC signal as a function of time. This enables us to connect the model with experimental measurements of the decay constants[46]. Or we may want to consider a case of constant excitation and look at the steady state behaviour of various populations[25].

Finally we emphasise that the rate equations reflect a choice of processes to be included and to be ignored. This is a pivotal decision discussed in Section 4.4 below.

4.4 How to establish key upconversion mechanisms in the rate equations

Setting up rate equations involves a decision which processes should be included. For example, in the most popular and Yb-Er sensitizer-activator pair, the arrangement of the energy levels enables several mechanisms including GSA/ETU (SA), GSA/ETU (AA), and even GSA/ESA. It is not clear a priori which UC mechanisms are the leading ones, but the measurement of the UC excitation spectrum may provide their fingerprints, for example it can be used to rule out GSA/ESA compared with GSA/ETU. In the first case successive absorptions in the GSA/ESA mechanism involve a combination of several energy levels of the activator ion in the resulting excitation spectra. In contrast, the GSA/ETU effect involves only the GSA levels in the sensitizer, so the whole excitation spectrum should arise from the sensitizer ion[30]. This is

illustrated in the 2%Er-18%Yb $NaYF_4$ and 2%Er $NaYF_4$ systems studied by Suyver *et al*.[27] In the Yb-Er co-dopant system, only a clear Yb^{3+} signature related to the electronic excitations into the $^2F_{5/2}$ and $^2F_{7/2}$ is recognised. This implies that the GSA/ETU (SA) is the leading process and directly proves that the excitation of all the upconversion emission bands is sensitized via Yb^{3+}. As indicated earlier, reasons include a large σ_{GSA} of Yb (one order of magnitude high than Er) and more efficient energy transfer Yb-Er than Er-Er due to around 10 times higher concentrations of Yb than Er[27]. For the 2% Er system, the excitation spectrum is distinctly different, showing multiple transitions, e.g., $^4I_{15/2} \rightarrow {}^4I_{1/2}$, and $^4I_{11/2} \rightarrow {}^4F_{7/2}$. In this case, excitation takes the form of successive absorption of pump photons by the single Er^{3+} ions, by the GSA/ESA mechanism[27]. Conversely, in a 10% Er-doped sample, Auzel *et al* have observed the multiphoton excitation spectra confirming the GSA/ETU (AA) mechanism instead of GSA/ESA[111]. The results suggest that as the energy transfer rate varies as R^{-6}, in materials with a single type of ion, such as Er^{3+}, the GSA/ESA mechanisms often dominate the upconversion processes in samples with low doping, whereas the GSA/ETU (AA) is dominant in highly-doped samples.

Another effective scheme to distinguish GSA/ESA and GSA/ETU is to record the time-dependent UC luminescence after a short (ns or less) excitation pulse[27]. The absorption in the ground and intermediate excited states in the case of GSA/ESA occurs on a less than nanosecond timescale, resulting in rapid onset of upconversion luminescence. The subsequent decay should show a single exponential curve after the excitation pulse (Fig. 7). In the case of GSA/ETU, the activators are excited via at least two subsequent energy transfer processes, which are much longer than the excitation pulse. Therefore, the population on the emitting levels gradually increases after the excitation pulse, so the UC lifetime decay first shows a rise (on a microsecond scale in common materials) reflecting the increasing population on the emitting level followed by an exponential decay. The resulting time-dependence of the UC reflects the decay rate of the excited state of the sensitizer, the energy transfer rate, and the decay rate of the emitting levels of the activator. In the case when GSA/ESA and GSA/ETU exist simultaneously in a system, the UC signal will show bi-exponential characteristics.

The UC decay characteristics can also help recognise energy diffusion. If diffusion of excitation occurs, then the excitation energy will migrate among sensitizer ions within the crystal lattice until a suitable activator ion is found. Since the sensitizer-activator ion pairs with the shortest separation have the highest energy transfer rates, an excitation gradient may be established within the crystal. If no diffusion occurs, the sensitizer-activator pair density distribution would favour pairs with the largest radial separation; pairs with shorter separations would be more likely to undergo cooperative energy transfer. One manifestation of this would be the non-exponential decay of UCL, reflecting the different transfer rates for different pair separations. The frequently observed exponential UCL decay at pulsed excitation indicates rapid energy diffusion. In this case spatial inhomogeneities of the sensitizer ions are effectively averaged out and the rate limiting step of direct energy transfer determines the time dependence of UCL. These examples

indicate that a combination of excitation spectra and decay time measurements are two useful methods to distinguish and determine the relative weight for various UC mechanisms.

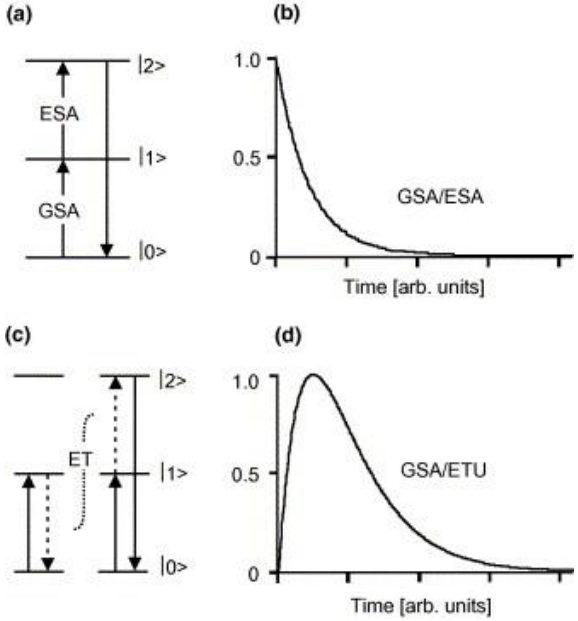

Fig. 7. Schematic representation of the GSA/ESA (a) and GSA/ETU (c) processes. Dotted and straight arrows represent nonradiative and radiative ET, respectively. The graphs in (b) and (d) describe the UCL time-evolution of the emission after a short excitation pulse, resulting from the two processes. Reprinted with permission from Suyver et al.[27] Copyright 2005, Elsevier.

4.5. Example application of rate equations: effect of nanocrystal size on UCL

The principal strategies for modifying properties of the UCL discussed earlier involve: (a) variation of the host lattice and (b) variation of type(s) and concentrations of dopant Ln^{3+} ions in the lattice and (c) modification of excitation conditions – wavelength and irradiance. However UCL can also be tuned by modifying the nanoscale morphology such as the size and shape of UCL-emitting nanostructures, and many experiments confirm that the UC luminescence decay characteristics and upconversion efficiency are size-dependent[45, 46, 112]. Changing size may dramatically influence the nonradiative properties (multiphonon relaxation and energy transfer), and changing the nanostructure shape may, in principle, influence the radiative and energy transfer processes. In particular, the ETU process in nanosystems is not only dependent on the initial distribution of the excited states, but also on the boundary conditions of the nanoparticles and material properties. Near the surface two additional mechanisms become important: one is the modification of the phonon density of states[17], another is the disordering in the surface layer in whose electronic and structural properties differ from that in the core. A simple approach to interpret size effects is to separate the transition and relaxation rates of all upconversion steps into surface and core contributions[46].

Our rate equation analysis in Section 4.4 links the observed decay rates to microscopic, molecular level parameters in the rate equations. The contributions of the nonradiative recombination mechanisms in the centre and near surface of nanocrystals are, generally, different. This makes it

possible to propose a quantitative model of the observed upconversion decay times which takes into account different material properties near the nanocrystal surface and within its volume[46]. This yields the relationship between the observed decay rates and nanocrystal size.
In this model, the nanocrystal is separated into the a spherical shell near the surface, of thickness *d* and a spherical core[88, 113]. The corresponding luminescence decay rates in the shell and in the core are denoted, respectively as W_s and W_c. The observed decay rate for each luminescence transition in the nanocrystal is given by a weighted average of the rates W_s and W_c with weights determined by the respective fractions of the shell and /core volumes, denoted F_s and F_c. In this way, the observed rate becomes a function of the nanocrystal's radius *R* and shell thickness:

$$W(\mathrm{R,d}) = \mathrm{W_s F_s} + \mathrm{W_c F_c} = \mathrm{W_s}\frac{\frac{4}{3}\pi\mathrm{R}^3 - \frac{4}{3}\pi(\mathrm{R-d})^3}{\frac{4}{3}\pi\mathrm{R}^3} + \mathrm{W_c}\frac{\frac{4}{3}\pi(\mathrm{R-d})^3}{\frac{4}{3}\pi\mathrm{R}^3} \quad (28)$$

Since the behaviour of the observed decay rates in smaller nanocrystals is dominated by the contribution from the near-surface decay rate which is generally higher than in the core due to higher defect density in the near-surface region, this model is able to describe a reduction of the decay time with decreasing size[113].

Now, we can also combine Eqn. (16) and Eqn. (28) to obtain an alternative expression for the photon emission rate as a dependency on *R* and *d* (via F_s and F_c) and the radiative and nonradiative decay times, τ_{rad} and τ_{nrad}:

$$\frac{N_1}{\tau_{rad}} = AN_0\left(\frac{W_{rad}}{W_{rad}+W_{s,nrad}F_s+W_{c,nrad}F_c}\right) \quad (29)$$

Since the surface fraction has a higher nonradiative decay rate ($W_{s,nonrad} > W_{c,nonrad}$), while W_{rad} is the same for either fraction, we can see that by reducing the nanoparticle size, and hence increasing F_s, the photon emission rate N_1/τ_{rad} will be reduced resulting in a lower UCL for smaller particles (if all other parameters are unchanged) .

4.6 Numerical solutions of the rate equations

Rational design of UC materials requires theoretical modeling because the relevant multidimensional parameter space cannot be probed accurately enough in practical experiments, despite recent availability of combinatorial high throughput material synthesis methods. Some level of insights concerning solutions of the rate equations can be obtained by using mathematical analysis. In some specific cases, with more assumptions, it might be possible to obtain analytical[25] or approximate solutions[114]. However, generally, solving these and other similar rate equations requires numerical simulations and this, in turn, requires the knowledge of all parameters. This is really challenging given their sheer number and the complexity of the underpinning mechanisms. A good source of these parameters is the area of solid state lasers where rate equations have been commonly utilised. Solid state laser materials have been designed

either to minimise the UC to promote more efficient laser action, or in the case of UC lasers, to optimise the UC[5, 6, 115].

The parameters in the rate equation are derived from optical experiments focusing on luminescence dynamics and steady state luminescence intensities for all transitions of relevance for UC. These transitions need to be selectively and individually excited[71, 116, 117]. A specific rate equations model is then proposed and its parameters adjusted to fit the experimental data. The parameters for the particular crystal-matrix combination determined in this way and those available from the literatures are supplemented with those measured for other similar crystals[118]. Additional adjustments to the parameters are made when the rate equations are applied to nanomaterials (with increased role of surface effects and modified energy transfer rates) but the parameters were taken from bulk crystals, with some having been modified by two orders of magnitude[118]. The accuracy of these parameters is difficult to determine and this affects the uncertainty of the simulated results.

Several groups demonstrated numerical solutions of the rate equations describing upconversion, including in Refs [71, 119-124]. These and other informative publications discussing rate equations are listed in Table 1. See original references for diagrams of the relevant transitions. Among the most advanced recent approaches was the modeling carried out in Ref.[71] aimed at funneling excitation energy into the most efficient UC transitions in $NaYF_4$: Er,Tm. Ref. [125] discussed a similar model in $NaYF_4$ Yb,Tm focusing on accurate description of energy migration. A detailed model of UC in the classic $NaYF_4$: Er,Yb has been presented in Ref.[120] although the focus was not on UC but on fundamental study of plasmon enhancement of energy transfer. The rate equations have been also used in Ref. [121] to understand the record 12% UC quantum yield in Er-doped Gd_2O_2S. Broadband upconversion was modelled in Refs. [122, 123]. We particularly highlight Ref.[124] in a classic material $NaYF_4$: Yb, Er where two different rate equation models have been carefully compared. These and other publications suggest that, despite challenges and limitations, the interest in further refining the rate equations for the UCL will continue.

Material	Comments	reference
$NaYF_4$:Yb^{3+}/Er^{3+}	The equations consider the $^2F_{5/2}$ and $^2F_{7/2}$ levels of Yb^{3+}, and the $^4S_{3/2}$, $^4F_{9/2}$, $^4I_{11/2}$, $^4I_{13/2}$, and $^4I_{15/2}$ levels of $Er3^+$.	120
Nd^{3+} doped ZBLAN glass ceramic	The model considers the first 15 states of Nd^{3+}	122
Nd^{3+} doped fluorozirconate glasses with $BaCl_2$ nanocrystals	The model considers the first 15 states of Nd^{3+}	123
β-$NaEr_{0.2}Y_{0.8}F_4$	The UC model considers ground state absorption, excited state absorption, stimulated emission, spontaneous emission, multi-phonon relaxation, energy transfer upconversion and cross-relaxation.	126
Er^{3+}-doped Gd_2O_2S	Limited to the $^4I_{15/2}$, $^4I_{13/2}$, $^4I_{11/2}$, and $^4I_{9/2}$ states of the Er^{3+} ion. Short pulse excitation. Only the ETU mechanism	121
$NaYF_4$, various lanthanide dopant pairs and other materials	Holistic rate equation modelling. All photophysical transitions. Rate constants calculated using the Judd–Ofelt theory for electric dipole emission, the energy gap law for multiphonon relaxation, and	127

	theories byKushida and Miyakawa and Dexter for phonon assisted ET.	
β-$NaYF_4$:Yb:Tm	The total system of equations combines the rate equations of all levels of every ion in the sample, no population averages.	[125]
YF_3:Yb:Tm	Two lowest levels of Yb, seven lowest states in Tm, back-transfer from Tm to Yb has been neglected, multiple other assumptions.	[116]
Brium-thorium fluoride glass with Yb:Tm and Yb;Er	Seven levels in Tm, six levels in Er, two levels in Yb, only cooperative upconversion. Analytical expressions for luminescence intensities under steady state conditions.	[8]
Fluoride glass doped with Yb:Tm and Yb:Ho	Modelled two-photon processes for $^3F_4 \rightarrow {}^3H_6$, $^2S_2 \rightarrow {}^5I_8$ transitions and three-photon processes for the $^1G_4 \rightarrow {}^3H_6$ transition	[128]
Various phosphors doped with Tb:Tm and Yb:Er	Seven states of Er and Tm, two states of Yb. Multiple assumptions.	[119]
β-$NaYF_4$:Yb:Er	A new mechanism involving Yb^{3+} to Er^{3+} energy transfer UC out of the green-emitting $^2H_{11/2}$,$^4S_{3/2}$ states	[124]
LaF_3:Tm	9 levels, 4 groups of transitions	[114]
Tm doped ZBLAN	6 levels, no energy transfer between pairs of ions	[115]
$NaYF_4$:Er^{3+}/Tm^{3+}	Incoming and outgoing rates of electric dipole and magnetic dipole radiative transitions, nonradiative multiphonon relaxation and energy transfer, 8 levels in Er, 7 levels in Tm	[71]
$NaYF_4$:Yb,Tm@$NaYF_4$	2 levels in Yb, 7 levels Tm, pulsed excitation.	[118]
Yb:Tm-doped KY_3F_{10}, $LiYF_4$ and BaY_2F_8	2 levels Yb, 6 levels Tm	[129]

Table 1. Overview of publications discussing rate equations.

5. Optical properties of upconversion luminescence at a nanoscale

5.1 Colour (emission spectrum)

The colour of UCL, is a result of the optical (radiative) transitions within the f-orbitals of the Ln^{3+} ions which are influenced by multiple processes, as explained in Sections 2 and 3. The eventual spectral shape of the emission spectrum is a result of a complex interplay between the population and depopulation of various emitting states. This, in turn, depends on the energy transfer rates influencing all intermediate states playing a role in the final emission. The relevant processes involve cross-relaxation, phonon-assisted energy transfer and resonant energy transfer and migration all varying with the inter-ion distance. Thus tuning the colour of UCL requires careful management of photophysical interactions between ions, to enhance or suppress specific mechanisms[130]. In this way, tuning desirable colour of UCNPs frequently involves engineering the relative intensities of multiple emissions or achieving a single emission band by balancing many photophysical processes. The most obvious way to influence the colour is by using different dopant Ln^{3+} ions, with different optical transitions, in the inorganic matrix (fluoride or oxide or alternative). For example, for the widely used host matrix β-$NaYF_4$ doped with sensitizer Yb^{3+} ions and Ln^{3+} activator ions, the UC emission appears green to the eye when co-doped with Yb/Er and blue when codoped with Yb/Tm ions[75]. In addition, the available radiative transitions result in additional red and NIR peaks in the emission spectra, respectively. Depending on the envisioned application, broad or narrow emission peaks can be desirable. Broad emission is for example advantageous for colour management of light sources[131]; controlled colour fine-tuning is

advantageous for display technology[48, 132], and narrow emission spectra in specified colours are useful for applications such as colour multiplexing in biological media[50] or security coding[133]. We will discuss the different strategies that have been developed in recent years to obtain emission covering a wide spectral range; colour tuning or single-band emission spectra.

5.1.1 Spectrally wide emission

As discussed earlier, individual Ln^{3+} activator ions have multiple energy levels which can be depopulated by radiative and nonradiative transitions. Choosing dopant/host combinations that allow the population of multiple emitting states, with comparable probability, results in spectra consisting of multiple bands which may overlap and form broad emissions. This may be desired in some applications, for example for the development of light sources.

Enhancing higher-order upconversion

Co-doping Yb^{3+} and Tm^{3+} in a $LiYF_4$ matrix yields emission bands spanning the UV, VIS and NIR regions with the dominant visible peaks in the blue region[134]. In addition, higher order three- and four-photon upconversion processes (emitting at 368, 450 and 480 nm) were amplified when the Yb-concentration was increased from 20 to 25 mol% unlike the red emission (at 650 nm), attributed to increased total energy transfer from Yb^{3+} to Tm^{3+}. However higher concentrations of Yb^{3+} induce UCL quenching, especially with respect to the higher order emissions[75]. Through rational design, Wang and co-workers have recently increased the efficiency of energy transfer between Yb^{3+} at high concentrations and Er^{3+}, resulting in enhanced four-photon upconversion and UC emission from the $^2H_{9/2}$ level of Er^{3+} at 407 nm[52]. In addition, the $^4F_{9/2} \rightarrow {}^4I_{15/2}$ (red emission) was enhanced, while the $^2H_{11/2} \rightarrow {}^4I_{15/2}$ and $^4S_{3/2} \rightarrow {}^4I_{15/2}$ (both green emissions) retained high emission rates as well, resulting in a broad emission spectrum in the blue, green and red regions (see Fig. 8). This increase in blue and red emission resulted from a novel design where the Yb-sensitizers are located in clusters throughout the host matrix, in an orthorhombic crystallographic structure in $KYbF_7$:Er (2 mol%) nanocrystals. This design facilitates $Er^{3+} \rightarrow Yb^{3+}$ back-energy-transfer from the $^4S_{3/2}$ level of Er^{3+} to the $^4F_{7/2}$ state of a nearby Yb^{3+}. Subsequently, the $^4I_{13/2}$ state thus populated produces red and blue emission as a result of the third and fourth energy transfer process, respectively (Fig. 8b). In addition to the broadening of the emission spectrum, this also resulted in an increase in brightness as discussed in Section 5.2.

Core-shell approach

The core-shell strategies have also been employed to cover a wide emission spectral range. Ye *et al.* recently broadened the emission spectrum by isolating the activator in the core from the sensitizer in the shell[135]. Their $NaYF_4$:Yb(50 mol%)@$NaYF_4$:Ho(1 mol%) nanocrystals exhibited emission peaks in blue, green and red regions resulting in an overall white appearance of the emission. In addition, the doping concentration of Yb in the core influenced the red/green emission ratio from 3 to 13 for 20 to 80 mol% Yb. Compared to non-core-shell counterparts the isolated activator/sensitizer structures showed slower decay rates and different emission spectra

peak ratios, which the authors attribute to strain-induced modifications of the crystal field in the active shells.

Introducing additional activators

Another way to extend the spectral range of the emission is by introducing additional activators, and thus additional emitting states, in the host matrix. As an example, Wang and Liu synthesized tri-doped $NaYF_4$:Yb,Tm,Er(20:0.2: [0.2-1.5] mol%) nanocrystals where multiple emitting states of Tm^{3+} and Er^{3+} were populated and their respective emission peaks covered the blue, purple, green and red colour bands[44]. The ratio between the peaks was tuned by increasing the Er^{3+} doping concentrations from 0.2 to 1.5 mol%, tuning the colour output from blue to white. More recently, Zhang *et al*., designed $NaGdF_4$:Yb,Tm,Er@$NaGdF_4$:Eu@$NaYF_4$ core-shell-shell nanoparticles resulting in a white colour output[48]. They also found that the emission could be further tuned by changing the excitation power density, as further explained in the following section.

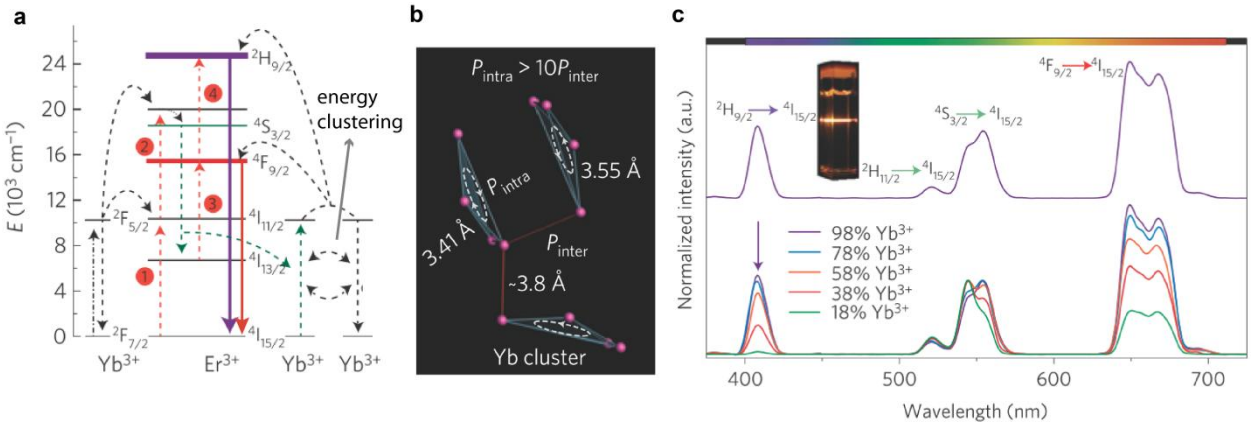

Fig. 8. Spectrally wide emission through the enhanced 3- and 4-photon upconversion process resulting from Yb-clustering. (a) Schematic of the proposed energy transfer mechanisms between Yb- ion clusters and Er-ions, leading to enhanced red (3-photon) and blue (4-photon) emissions. The dashed-dotted, dashed, dotted and full arrows represent photon excitation, energy transfer, multiphonon relaxation and emission processes, respectively. (b) Excitation energy clustering by Yb^{3+} tetrad clusters in orthorhombic-phase $KYbF_7$. (c) Resulting emission spectra from $KYbF_7$:Er(2 mol%) nanocrystals (top), and for $KYbF_7$:Er,Lu(2, [0-80] mol%) crystals where Yb^{3+} is replaced by Lu^{3+} in increasing concentration (bottom), excited by 980 nm at 10 W/cm^2. The spectra were normalized for green Er^{3+} emission. The inset shows a photograph of $KYbF_7$:Er (2 mol%) nanocrystal luminescence. As can be seen, the red and blue peak (4 and 5-photon process) increase with increasing concentration of Yb^{3+}. Reprinted with permission from Wang *et al.*[52]. Copyright 2014, Nature Publishing Group.

5.1.2 Colour tuning

Emission spectra with multiple emission bands can be further fine-tuned to specific ratios for the optical transitions, and to yield a spectrum corresponding to a desired colour.

Red/green emission ratio

Fine-tuning of the emission spectrum has been widely achieved in the case of the red and green emission bands of Er^{3+} and Ho^{3+} ions[136-138]. By increasing the concentration of Yb^{3+} from 0 to 15

mol% in Gd_2O_3 hosts Liu *et al.* employed the phonon-assisted increased back-energy-transfer rates from Er^{3+} to Yb^{3+} to obtain tuneable emission spectra[43]. At 0 mol% the green emission dominated, while at 15 mol% the red emission was dominant. Punjabi *et al.* synthesized α-$NaYF_4$:Yb,Er(80:2 mol%)@CaF_2 where the addition of the CaF_2 shell resulted in a 15 times stronger red emission peak as compared with β-$NaYF_4$:Yb,Er(20:2 mol%)@$NaYF_4$[139]. In addition, the doping concentration of Yb^{3+} influenced the red/green emission ratio from 1 to 2 for 20 to 98 mol% Yb. The high Yb-concentration resulted in higher population of the red $^4F_{9/2}$ emitting state of Er^{3+} again due to back-energy-transfer between Yb^{3+} and Er^{3+} ions, and the thick CaF_2 shell prevented quenching of the absorbed energy.

A low red/green luminescence ratio has been achieved by a judicious choice of dopants in a $NaYF_4$ matrix[42]. By co-doping Er^{3+} and Sm^{3+}, the intermediate states that populate the red emitting states of Er^{3+} ($^4F_{9/2}$) were quenched by nonradiative energy transfer to Sm^{3+}, see Fig. 9. Energy transfer from $^4I_{11/2}$ and $^4I_{13//2}$ levels of Er^{3+} to the available manifolds in Sm^{3+} reduce the population of these states by a factor of 10 and 70, respectively, resulting in a red/green ratio of ~0.25. As red emission is dependent on both the $^4I_{11/2}$ and $^4I_{13//2}$ population, while green only on the $^4I_{11/2}$ population this results in dominant green emission in Er/Sm-doped $NaYF_4$ crystals. As Sm^{3+} dissipates this energy via multiphonon relaxation there is no enhancement of green emission, only quenching of red emission.

Besides doping concentration, the size, crystallinity and shape[137, 140] and excitation power density[141] also influences the red/green ratio, especially when nonradiative recombination plays a significant role.

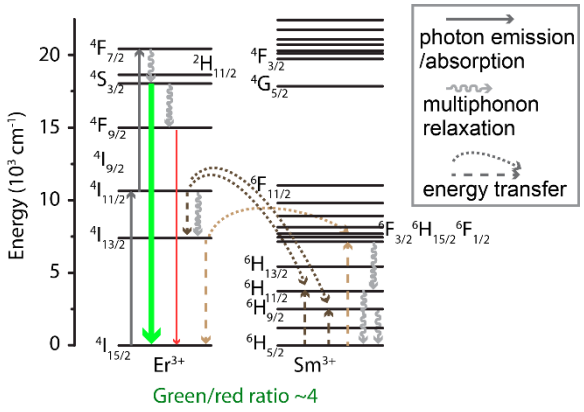

Fig. 9. Co-doping Er3+ with Sm3+ in $NaYF_4$ crystals results in a green/red emission ratio of 4, due to quenching of the red emitting states of Er^{3+} by Sm^{3+}. Reproduced from Chan *et al.*[42]. Copyright (2012) American Chemical Society. We made a minor correction by inserting the (brown) energy transfer arrows for the Er $^4I_{13/2} \rightarrow$ Sm $^6F_{3/2}$ $^6H_{15/2}$ $^6F_{1/2}$ transition for completeness.

Colour tuning by excitation

For some applications it might be desirable to tune the colour output of a material with a fixed composition of both core and shell materials including the dopants, for example in (three-dimensional) display technology or data storage. To achieve this, Deng *et al.* varied the excitation

wavelength (980 nm and 808 nm) and pulse width (980 nm, 200 μs - 6 ms) to tune the colour ratio of NaYF4-based core-shell nanocrystals[47]. In this strategy, the core was doped with Nd/Yb; the first shell - Yb/Tm; second shell - undoped; third shell - Yb/Ho/Ce; and the outer shell again was undoped. Under 808 nm excitation the energy absorption by Nd^{3+}, subsequent energy transfer to Yb^{3+} and sequential energy transfer from Yb^{3+} to Tm^{3+} results in blue emission. Under 980 nm excitation, the Yb/Ho/Ce system is active. As established earlier[45-47], the Yb^{3+} sensitizers transfer the energy to the Ho^{3+} activators that possess a green and a red emitting state, while Ce^{3+} ions mediate the cross relaxation from (intermediate) green emitting states to (intermediate) red emitting states of Ho^{3+}, enhancing the red emission. Importantly, Deng *et al.* demonstrated that the contribution of the red emitting state is highly dependent on the excitation pulse width. At steady-state conditions (> 5 ms pulse width) the red/green ratio was ~8, independent of pump power, but decreasing the pulse-width gradually reduced this ratio, down to 0.5 for 200 μs pulses. This phenomenon is ascribed to the fairly slow non-radiative cross relaxation of Ho^{3+} green to red emitting states, which need sufficiently long excitation pulses durations in order to become noticeably populated. Thus, by using two different excitation wavelengths and other than steady state excitation conditions the emission spectra were engineered to cover the full visible spectrum, see Fig.10 (a) and (b). As previously mentioned, Zhang *et al*. engineered white core@shell@shell UCNPs by doping six kinds of lanthanides: $NaGdF_4$:Yb,Tm,Er @$NaGdF_4$:Eu@$NaYF_4$ in the core@shell@shell structure[48], with the doping concentrations 50, 0.05, 0.5, 10 mol% for Yb^{3+}, Tm^{3+}, Er^{3+} and Eu^{3+}, respectively. The white colour was present at 15 W/cm^2 and by changing the excitation power density from 3 to 30 W/cm^2 they were able to dynamically tune the colour output from green to purple, as shown in Fig. 10 (c) and (d). With increase of excitation density all emission bands increased in intensity but with a different rate, leading to different final colours. The fine-tuning is due to early saturation of the limited amount of Er^{3+} activators (green emission), followed by an increase in blue emission from Tm^{3+} and, finally, a higher-order energy transfer from Tm^{3+} *via* Gd^{3+} to Eu^{3+} generates red emission from Eu^{3+} at high excitation density.

Colour tuning by energy migration

Geometric separation of ions holding different functions in the upconversion process to achieve colour tuning was introduced by Liu's group[54, 55]. The functional ions identified as sensitizers, accumulators, migrators and activators were doped in multiple separate shells to realize energy migration-mediated upconversion, as schematically drawn in Fig. 2d. In this work, Yb^{3+} and Tm^{3+} ions in the core sensitize and accumulate the absorbed energy respectively. The Tm^{3+} ion successively accumulates energy from Yb^{3+} ions, and when 5 of such energy transfers have occurred (5 excitation photons), it can transfer this energy from its $^1I_6$ state to the $^6P_{7/2}$ of Gd^{3+}. The Gd^{3+} ions in the migration shell facilitate fast energy transfer to the high $^6P_{7/2}$ energy state, with low probability of energy loss by multiphonon or cross-relaxation processes due to the large energy gap to the ground state (~3.2 x 10^4 cm^{-1}). This energy eventually reaches the outer shell doped with activators resulting in the population of their emitting state. Due to the accumulation and efficient migration of the absorbed energy, the last energy transfer step to the activator can be

single-step which means the requirement for activators with long-lived intermediate states is alleviated. Wang *et al.* showed that emission spanning the visible spectrum from activators such as Tb^{3+}, Eu^{3+}, Dy^{3+} and Sm^{3+} was feasible, whereas otherwise anti-Stokes emission from these ions would only be possible at high $I_{ex} \sim 10^6$ W/cm^2 or extremely low temperatures.

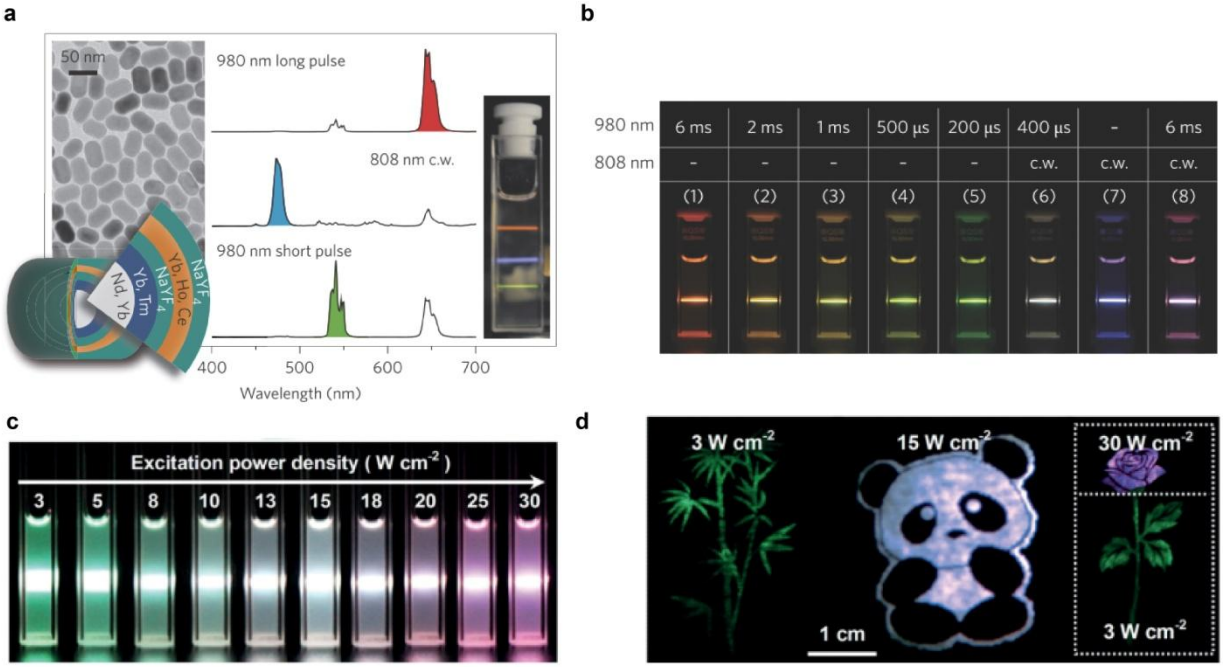

Fig. 10. Colour tuning of UCNPs with a fixed composition based on pulse duration (a and b) or excitation power density (c and d). (a) TEM image and schematic design of core-shell UCNPs with multiple dopants (left), and their emission spectrum for 3 different excitations: 6 ms pulse at 980 nm, 200 µs pulse at 980 nm, and continuous wave 808 nm excitation. The red green and blue emission from a solution of these particles is shown in the photograph in the inset. Other excitation schemes resulted in the colour output as depicted in (b). In (c), the tuneable colour output from $NaGdF_4$:Yb,Tm,Er @$NaGdF_4$:Eu@$NaYF_4$ core@shell@shell UNCPs is shown when excited with different power densities. The nanoparticles were combined with colourless ink and printed on paper to display several images in different colour (excitation density) as shown in (d). Panel a and b: Reprinted with permission from Deng *et al.*[47].Copyright 2015, Nature Publishing Group. Panel c and d: Reprinted with permission from Zhang *et al.*[48]. Copyright 2015, Wiley-VCH Verlag GmbH & Co. KgaA.

5.1.3 Single-band emission spectra

Strategic co-doping with lanthanide or metal ions

Single-band emission can be obtained by increasing the depopulation rate of intermediate states responsible for the unwanted emissions, while, ideally, at the same time using this energy to increase the population of the intermediate state of the desired radiative energy states. This can be achieved by strategic co-doping with selected ions, whose energy gaps match non-radiative transitions necessary to depopulate the unwanted and populate the desirable emitting states. Chen *et al.* used this strategy to increase the red/green ratio by triple doping $NaYF_4$:Yb/Ho (20:2 mol%) with Ce^{3+} ions, which facilitate the cross relaxation from the Ho^{3+}-green emitting state ($^5S_2/^5F_4$) or the green intermediate state ($^5I_6$), to the Ho^{3+}-red emitting state ($^5F_5$) or the red intermediate state ($^5I_7$), respectively, to promote red emission[142], see Fig.11a. At 15% Ce^{3+} doping

the red/green ratio was ~11, however the green peak never completely disappeared. More recently, a 30% doping of Ce^{3+} with Ho^{3+} and Yb^{3+} in the core of active-core@active-shell NPs increased the red/green ratio to > 20, although in expense of the emission brightness due to cross relaxation from the red emitting $^5F_5$ state in Ho^{3+} to Ce^{3+} as well, see Fig. 11a [143]. Wang *et al.* obtained pure red, red and NIR emission by synthesizing nanocrystals consisting of a $KMnF_3$ host co-doped with either Yb/Er (18:2 mol%), Yb/Ho (18:2 mol%) or Yb/Tm (18:2 mol%), respectively[144]. The complete disappearance of the blue and green emissions is a result of the non-radiative energy transfer from the green ($^4S_{3/2}$) and blue ($^2H_{9/2}$) emitting state of Er^{3+} to the $^4T_1$ level of Mn^{2+}, which in turn transferred energy non-radiatively to the red emitting state ($^4F_{9/2}$) of Er^{3+}(Fig. 11b). Similar energy transfers to the red and NIR emitting states of Ho and Tm were suggested for the Yb/Ho and Yb/Tm co-doping pairs, which resulted in single-band emission spectra of the UCNPs (Fig. 11 (c) and (d)). Moreover, this single-band feature was independent of the dopant concentration (in the Yb/Er range [0-18]/[2-5] mol%) and of the pump power. The extremely efficient exchange-energy transfer process between the lanthanide Er^{3+} and transition metal Mn^{2+} ions was possible thanks to advances in the oil-based synthesis procedure which ensured homogeneous high doping of Ln^{3+} ions into the $KMnF_3$ host lattice. An alternative method to facilitate red emission through non-radiative energy transfer between Er^{3+} and Mn^{2+} was presented by Tian *et al.*[145], who introduced high concentrations of Mn^{2+} ions into the $NaYF_4$ host lattice, additionally doped with Yb/Er (18:2 mol%). They demonstrated that the higher the concentration of Mn^{2+} the more energy was transferred to the red emitting states at the expense of green and blue emitting states. At the highest concentration of 30% Mn^{2+} the emission showed a single red peak, independent of Yb-doping concentration ([0-28] mol%), pump power and temperature. Similar enhancement of red emission has been attributed to energy transfer between Er^{3+} and Tm^{3+} ions doped in $NaYF_4$. [42]. The authors explain the 50 times enhancement of the red emission by energy transfer taking place from the $^4I_{11/2}$ and $^4I_{13//2}$ levels of Er^{3+} *via* the $^3F_4$ level of Tm^{3+} back to the red emitting $^4F_{9/2}$ level of Er^{3+} in an ETU process (see Fig. 11e). Because both the $^3F_4$ level of Tm^{3+} as well as the $^4T_1$ level of Mn^{2+} have a large energy difference with the ground state (5800 cm^{-1} Tm^{3+}, >17 000 cm^{-1} Mn^{2+} [146]) multiphonon relaxation to the ground state is essentially prohibited and the excitation energy available for further energy transfer. This strategy not only results in the reduction of unwanted emission peaks but also in the enhancement of the desired emissions.

An efficient strategy thus entails that the strategic ion responsible for depopulating unwanted states has a low probability to lose the energy (e.g. via multiphonon relaxation to ground state) and instead recycles this energy to desired wavelengths[42, 71, 144, 145]. If this is not the case, there can still be promotion of desired wavelengths as long as the desired wavelength energy is lower (e.g. red vs green) and low energy phonon relaxation results in population of this state[142]. Both strategies have only been demonstrated for purifying red emission. In the case of the higher laying green emission state the only strategy reported so far is the quenching of red emission, without the ability to recycle this energy[42].

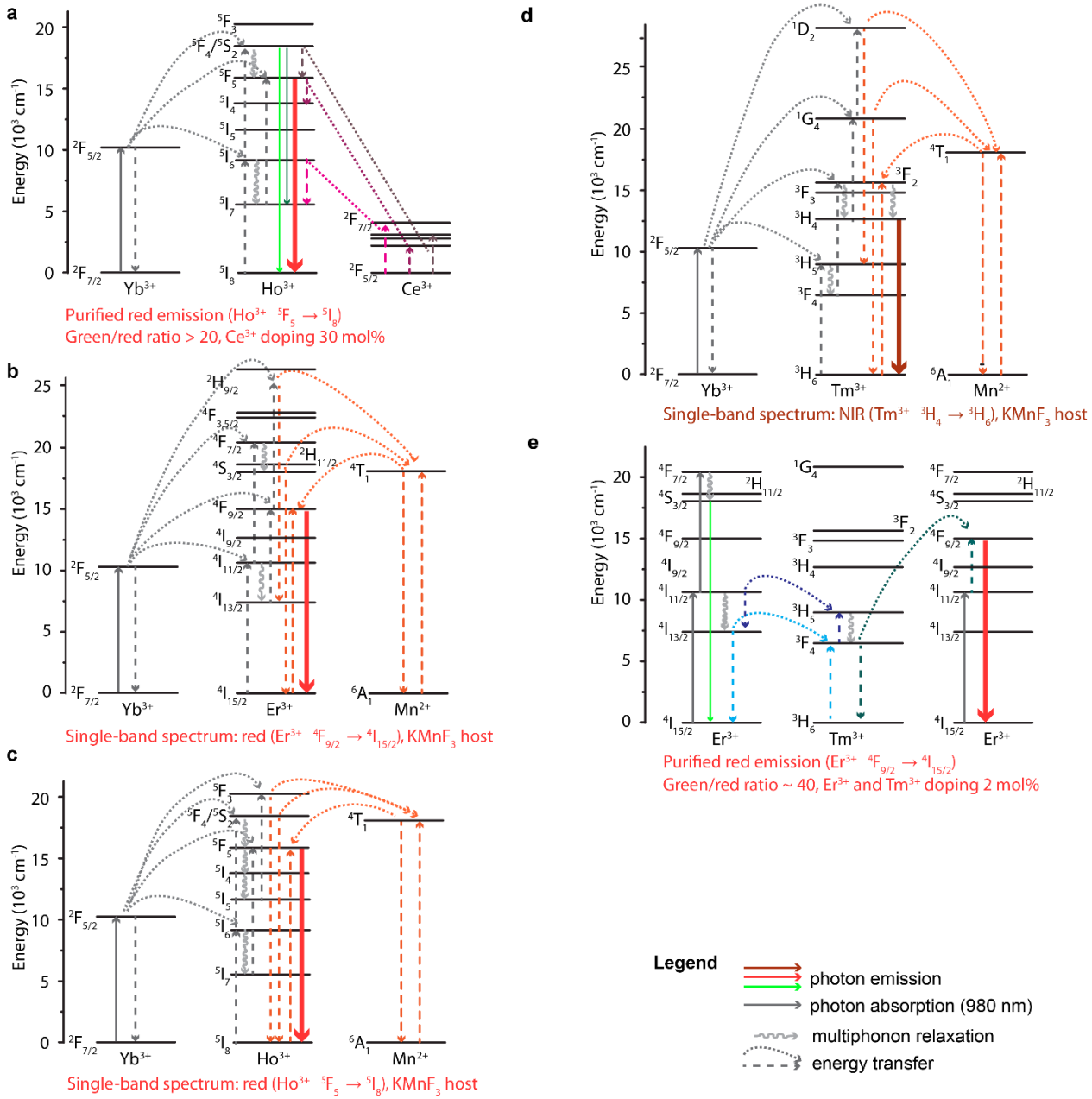

Fig. 11. Energy diagrams showing different strategies to obtain single-band emission spectra. (a) Co-doping Ho^{3+} with Ce^{3+} results in non-radiative energy transfer processes in favour of radiative red emission[142, 143], while co-doping Er^{3+} (b), Ho^{3+} (c) or Tm^{3+} (d) in a $KMnF_3$ host results in non-radiative energy transfers in favour of red, red and NIR emissions, respectively[144]. Co-doping Er^{3+} and Tm^{3+} in $NaYF_4$ resulted in purified red emission for doping concentrations of 2% each [42]. In (e) we made a minor correction with respect to Ref.[42] by inserting the (blue) energy transfer arrows for the Er $^4I_{13/2} \rightarrow$ Tm $^3F_4$ transition for completeness.

Strategic changes in host matrix

Colour purification can also be achieved by judicious changes in the host matrix. To purify the red emission peak, Dong *et al.* modified the local structure of lanthanides in cubic $Na_xLnF^{3+}{}_x$

nanocrystals by tuning the Na/Ln and F/Ln ratios to synthesize nonstoichometric nanocrystals[147]. As the Na/Ln and F/Ln ratios reduced, the red/green ratios increased, leading to highly purified red emission. For example, the red/green ratio varied from 1.9 to 71 for $Na_xYF^{3+}{}_x$ hosts and 1.6 to 116 for $Na_xGdF^{3+}{}_x$ hosts both doped with Yb^{3+} and Er^{3+}. The authors found that moderate amounts of Na^+ and F^- vacancies should appear when the Na/Ln and F/Ln ratios reduce, which results in lattice shrinkage (decreased lattice parameters were obtained from XRD measurements), decreased coordination number of Y^{3+} (or other Ln^{3+} in the Ln-F shell) and lower local symmetry around luminescent centres. As discussed in Section 2.2 a lower local symmetry strengthens the crystal field effects, which increased the overall brightness. It also influenced the purity of red emission, by facilitating cross-relaxation to depopulate (intermediate) green emitting states and simultaneous population of (intermediate) red emitting states in Er^{3+}. A further addition of a CaF_2 shell promoted the red emission by another 450 times, to enhance it suitability as a contrast agent in a biological context.

Absorbing dyes

Another strategy to modify spectral properties of the UCL is to quench unwanted radiation is by coating the UCNPs with an extra layer of highly absorbing dye in the unwanted spectral region, while leaving the desired colour unabsorbed. Zhou *et al.* followed this approach by synthesizing core-shell UCNPs with bright emission in the desired colour band by selecting appropriate dopant-host combinations, and subsequently, coating the particles with absorbing dyes to further eliminate the unwanted emission peak[50]. To achieve this, the core-shell UCNPs were first coated with a pure silica spacer layer, to prevent fluorescence resonance energy transfer (FRET) between fluorescent dye and the filtered upconversion band. The second coating layer consisted of silica doped with amino-reactive organic dyes. To obtain single-band green and single-band blue emission, nickel (II) phthalocyanine-tetrasulfonic acid tetrasodium salt (NPTAT) organic dyes were used, with an absorption maximum at 657 nm to filter the red emission band from Er-doped (green) respectively Tm- doped (blue) UCNPs. To obtain single-band red emission the absorbing dye rhodamine B isothiocyanate was used to filter the green emission. Coating with the dye-doped silica layer did not result in a significant alteration of emission lifetimes or a change in the slope of the log-log plot of excitation density versus emission intensity. Furthermore, the photostability of the UCNPs was not compromised and the optical absorption peaks of the organic dyes were maintained under long duration illumination with 980-nm as well using xenon lamp illumination. Fig. 12 illustrates the synthesis strategy, colour coding and multiplexed cell labelling applicability of these UCNPs. Zhou *et al.* further pursued the specific labelling of three different receptors associated with breast cancer cells, and demonstrated the advantages of using UCNPs for background-free multiplexed quantitative immunohistochemical identification of breast cancer.

To summarize, fine tuning of the UCL emission wavelengths can be achieved by changing the location, geometry, concentration and selection of the lanthanide ions, in addition to selecting appropriate host lattices and mediation by transition metal ions such as Mn^{3+}. The mechanisms

include changing the energy transfer distances, introducing additional energy transfer/cross-relaxation energy levels, and incorporating energy extractors or passivators other than the lanthanide ions[148]. Surface plasmon resonance processes, or excitation power dependencies can also influence colour, though usually are employed for UCL-brightness enhancement and will be discussed in the next section.

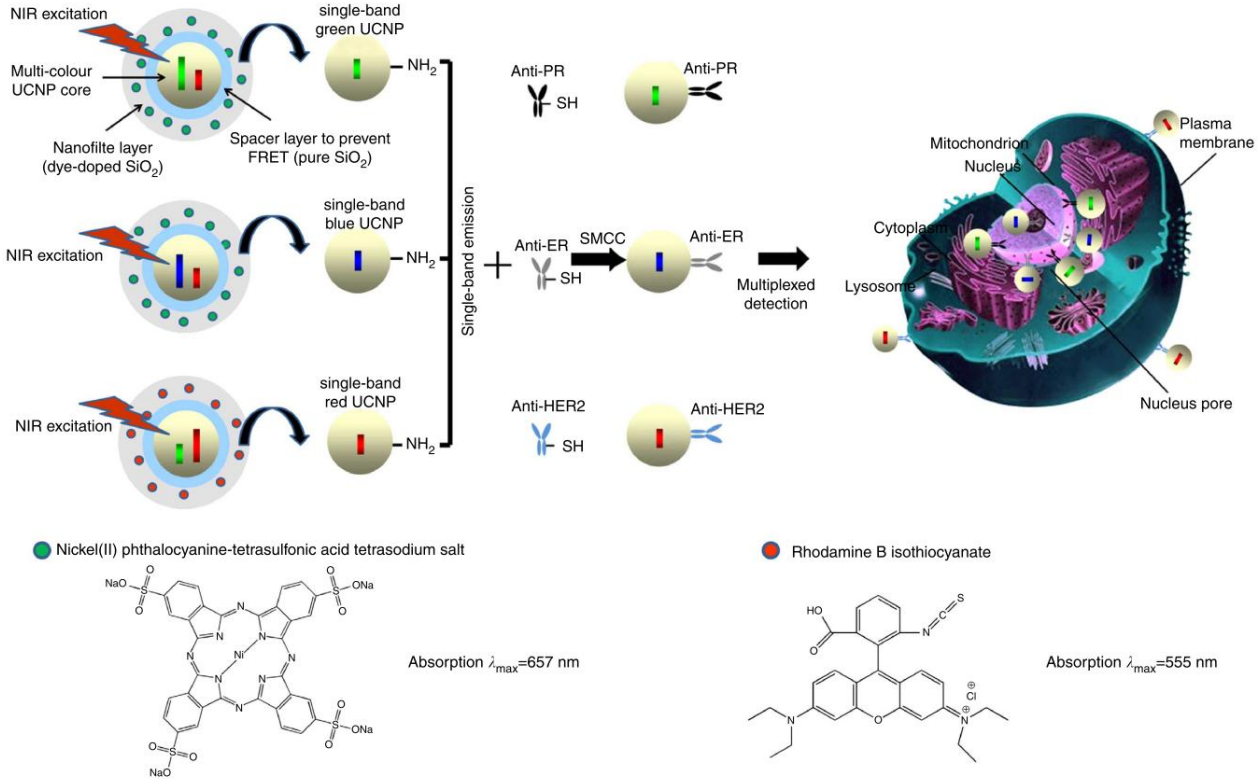

Fig. 12. Colour purification by coating UCNPs with highly absorbing dyes (molecular structures are shown). The resulting single-band UCNPs were further modified with antibodies (anti-PR, anti-ER and anti-HER2) to breast cancer biomarkers PR, ER and HER2, respectively. Colour multiplexed *in situ* molecular mapping of breast cancer biomarkers is schematically shown on the top right. Reproduced from Zhou *et al.*[50] under the Creative Commons (CC BY) licence.

5.2 Intensity and conversion efficiency

Lanthanide transitions and multiple-step upconverting processes generally lead to relatively low upconversion intensity and conversion quantum yield[119]. However, due to their unique optical properties they are intensely investigated in the context of application to life sciences, security and display technologies, and photovoltaics. For example, the signal-to-background ratios obtained using UCNPs outperforms that of alternative fluorescent nanoparticles in biomedical imaging[149]. Thus, the enhancement of the upconversion intensity is a key target to develop meaningful applications of upconversion, for example in biomedical deep tissue imaging[150].

Historically, the key approach here was the discovery of cooperative upconversion which has, for the first time, allowed a higher fraction excitation energy to be funnelled into the upconverting

activator centres[30]. This approach centres at maximising the absorption of the lanthanide sensitizer ions. These sensitizer ions are chosen to have a ground-state absorption cross-section, $\sigma_{GSA,}$ that is higher than the corresponding quantity in the activator ions. Additionally, their absorption coefficient α_{GSA} is also maximised by increasing the ion density N ($\alpha_{GSA} = N\sigma_{GSA}$)[151-154]. A typical example of such strongly absorbing sensitizer ion is Yb^{3+}, frequently used with activators such as Er^{3+}, Tm^{3+}, or Ho^{3+}, to increase their upconversion brightness. Yb^{3+} ion has an extremely simple energy structure in the VIS–NIR region: the ground state $^2F_{7/2}$ and the excited state $^2F_{5/2}$, separated by 10 000 cm^{-1} . The absorption of Yb^{3+} due to the $^2F_{7/2} \rightarrow {}^2F_{5/2}$ transition occurs at about 980 nm. The corresponding σ_{GSA} (1.2×10^{-20} cm^2) is large compared with the absorption cross section of the Er^{3+} ion (1.7×10^{-21} cm^2) at 980 nm excitation[155]. Recently, Nd^{3+} has become another popular sensitizer for UCNPs. The Nd^{3+} ions have multiple NIR excitation bands at shorter wavelengths such as 730, 808, and 865 nm, with large absorption cross sections, e.g., 5.1×10^{-29} cm^2 at 808 nm[156-158]. Both sensitizers and their absorption energy levels are shown in Fig. 13.

The concentration of sensitizer ions is usually chosen to be much higher than that of activator ions to maximise absorption of the excitation energy. For example, at weak excitation conditions (<100 W cm^{-2}) the Yb^{3+} doping is usually optimised to be within the 20~40% molar concentration range. This is much higher in comparison to typical doping levels of 1~2% for Er^{3+} and 0.2~0.5% for Tm^{3+} activator dopants. In most cases, an intensity decrease could be observed when the doping levels of Yb^{3+} ions are above the optimal threshold (in the weak excitation irradiance regime < 100 W cm^{-2}). This is attributed to back energy transfer from activators to sensitizers[159, 160] and/or nonradiative energy reabsorption between Yb^{3+} ions.

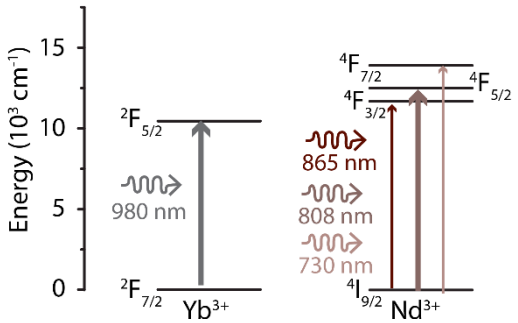

Fig. 13. Schematics of the energy levels taking part in GSA by two commonly used sensitizers, Yb^{3+} and Nd^{3+}.

The introduction of cooperative upconversion was a breakthrough in the field of UCL and it has led to a variety of new materials including nanoparticles with ever increasing upconversion brightness and other desirable features such as small nanoparticle size or unique characteristics at high pumping levels[25]. Progress in this field is continuing, due to critical significance of upconversion brightness for its applications. Here we summarise the approaches to UCL brightness including an overview of reported conversion efficiencies, followed by the discussion of strategies to further enhance the upconversion intensity.

5.2.1 Conversion efficiency and quantum yield

In order to objectively quantify the brightness of UCNPs one needs to quantify the UCNP's ability to absorb excitation light, and subsequently, convert this energy to emit photons in the desired wavelength. The first is governed by the absorption coefficient of the UCNP, that is the combined absorption cross section and concentration of the sensitizer ions, as explained in the previous section. The second is given by the conversion efficiency (CE), or quantum yield (QY), and we emphasise that these two terms are differently defined. Measurement of the absolute quantum yield of luminescent materials is described in[161, 162]. Conventionally, in fluorescent photoluminescence, the term quantum yield is used which is defined as[163]:

$$\mathrm{QY} = \frac{\#\text{photons emitted}}{\#\text{photons absorbed}} \tag{30}$$

In the case of UC, this means that a two-photon process can have a maximum QY of 50%, while a 3-photon process can have a maximum QY of 33%. Normalizing this value by multiplying by 2 or 3 has been suggested[27, 164], but the complex multiphoton excitation pathways in upconversion make this approach tricky. The parameter 'conversion efficiency' on the other hand is defined as[119]:

$$\mathrm{CE} = \frac{\text{power emitted, } P_{em}[\mathrm{W}]}{\text{power absorbed, } P_{abs}[\mathrm{W}]} \tag{31}$$

By taking the quotient of the respective powers, the CE more adequately reflects the net output of the upconversion process. Of course, the QY and the CE can be derived from each other by the emission respectively excitation spectra and photon energies via $E_{ph} = h\nu$.

The functional dependency of the CE (or QY) on excitation intensity, I_{ex} in W/cm^2, adds another complexity to its measurement. For a 2-photon process the CE generally increases linearly with excitation density (since $P_{em} \sim I_{ex}^2$) until the emitting energy level population starts saturating, resulting in saturation of the CE. However, the majority of articles that report the QY/CE only do this for a single I_{ex}, ignoring the functional power density dependency.

To measure the QY/CE of high refractive index samples, such as UCNPs, one needs to take into account the influence of angular distribution of photoluminescence emission, and scattering of excitation light resulting in a higher chance for absorption. A suggested method is the use of the integrating sphere[112, 119], which spatially integrates the internal light resulting in the measurement of the emitted as well as the absorbed light independent of scattering by the sample (see Fig. 14a), and recently a simplified measurement scheme has been proposed[165]. The integrating sphere method involves an elaborate set-up and calibration procedure, which might be the reason why absolute CE measurements of UCNPs are reported scarcely in literature. In Table 2 we summarized the thus far reported values of absolute CE or QY using integrating sphere measurements. In Fig. 14b we plotted the reported literature values versus size and I_{ex}.

The UCL brightness is an important but complicated parameter to quantify across different studies. In different excitation density regimes the competition between energy absorption, energy transfer, surface and concentration quenching ultimately defines the brightness. The balance of this competition can be influenced by different strategies, as discussed next.

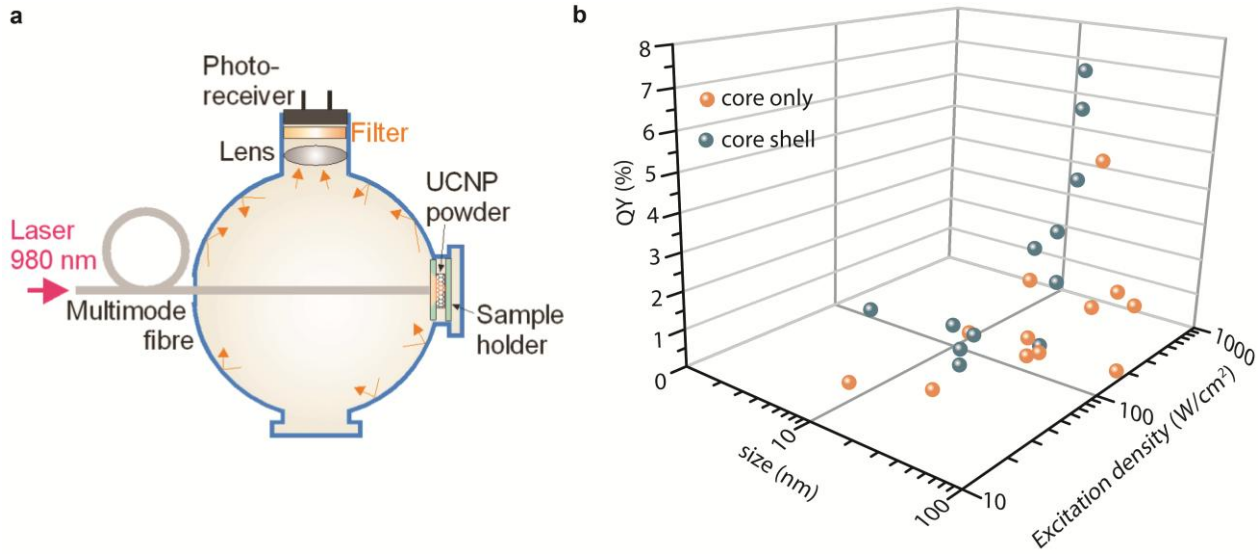

Fig.14. Measurement of absolute QY or CE. (a) General setup of integrating sphere measurement. Reprinted with permission from Zhao et al.[46]. Copyright 2013, Nature Publishing Group. (b) Reported literature values for absolute QY as a dependency of size and I_{ex} from table 2, excluding values from ref.[42].

Material	Core-shell	size	CE or QY [%]	I_{ex}	Ref
$NaYF_4:Yb_{0.18},Er_{0.02}$	no	Micron sized	CE [0.05 - 4]	[0.04 - 200] W/cm^2	Page *et al.*[119]
$NaYF_4:Yb_{0.27},Tm_{0.001}$	no	Micron sized	CE [0.004 - 2]	[0.15 - 1000] W/cm^2	Page *et al.*[119]
$NaYF_4:Yb_{0.2},Er_{0.02}$	no	100 nm	QY 0.30±0.10	150 W/cm^2	Boyer *et al.*[112]
$NaYF_4:Yb_{0.2},Er_{0.02}$	no	30 nm	QY 0.10±0.05	150 W/cm^2	Boyer *et al.*[112]
$NaYF_4:Yb_{0.2},Er_{0.02}$	no	8-10 nm	QY 0.005±0.005	150 W/cm^2	Boyer *et al.*[112]
$NaYF_4:Yb_{0.2},Er_{0.02}@NaYF_4$	yes	30 nm	QY 0.30±0.10	150 W/cm^2	Boyer *et al.*[112]
$NaLuF_4:Gd_{0.24},Yb_{0.2},Tm_{0.01}$	no	<10 nm	QY 0.47±0.06	17.5 W/cm^2	Liu *et al.*[166]
$NaYF_4:Yb_{0.2},Er_{0.02}$	no	5.4 nm	QY 0.0022±0.0001	10^3 W/cm^2	Ostrowski *et al.*[167]
$NaYF_4:Yb_{0.2},Er_{0.02}@NaYF_4$	yes	9 nm 5@2 nm	QY 0.18±0.01	10^3 W/cm^2	Ostrowski *et al.*[167]
$NaYF_4:Yb_{0.2},Er_{0.02}$	no	37 nm	QY 0.14±0.01	10^3 W/cm^2	Ostrowski *et al.*[167]
$NaYF_4:Yb_{0.25},Tm_{0.003}@NaYF_4$	yes	42 nm	QY	[0.02 - 78]	Xu *et al.*[168]

		30@6 nm	[0.04 - 3.5]	W/cm^2	
$NaYF_4$:$Yb_{0.2}$,$Er_{0.02}$	no	70 nm	CE [0.1 - 1.9]	[1 - 230] W/cm^2	Nadort *et al.*[145]
$NaYF_4$:$Yb_{0.25,}Tm_{0.003}$	no	33 nm	QY [0.45 - 0.91]	[1.3 - 20] W/cm^2	Liu *et al.*[165]
$NaYF_4$: $Yb_{0.25,}Tm_{0.003}$@$NaYF_4$	yes	43 nm 33@5 nm	QY [1.2 - 2.6]	[3.8 - 20] W/cm^2	Liu *et al.*[165]
$NaYF_4$:$Yb_{0.2,}Tm_{0.005}$	no	40 nm	CE [1 – 5]	[3 - 300] W/cm^2	Zhao *et al.*[25]
$NaYF_4$:$Yb_{0.2,}Tm_{0.04}$	no	40 nm	CE [0.4 – 1]	[3 - 300] W/cm^2	Zhao *et al.*[25]
$NaYF_4$:$Er_{0.1}$	No	Unknown	QY 0.9±0.2	10 W/cm^2	Chan *et al.*[42]
$NaYF_4$:$Er_{0.1}$,$Tm_{0.05}$	No	Unknown	QY 1.3±0.5	10 W/cm^2	Chan *et al.*[42]
$NaYF_4$:$Er_{0.1}$,$Pr_{0.05}$	No	Unknown	QY 0.04±0.02	10 W/cm^2	Chan *et al.*[42]
$NaYF_4$:$Yb_{0.8}$,$Er_{0.02}$@CaF_2	yes	26 nm	QY 3.2±0.1	10 W/cm^2	Punjabi *et al.*[139]
$LiLuF_4$:$Yb_{0.2}Er_{0.01}$	no	28 nm	QY 0.11	127 W/cm^2	Huang *et al.*[169]
$LiLuF_4$:$Yb_{0.2}Er_{0.01}$@ $LiLuF_4$	yes	40 nm 28@6nm	QY 3.6	127 W/cm^2	Huang *et al.*[169]
$LiLuF_4$:$Yb_{0.2}Er_{0.01}$@ $LiLuF_4$	yes	51 nm 28@11nm	QY 5.0	127 W/cm^2	Huang *et al.*[169]
$LiLuF_4$:$Yb_{0.2}Tm_{0.005}$	no	28 nm	QY 0.61	127 W/cm^2	Huang *et al.*[169]
$LiLuF_4$:$Yb_{0.2}Tm_{0.005}$@ $LiLuF_4$	yes	51 nm 28@6nm	QY 6.7	127 W/cm^2	Huang *et al.*[169]
$LiLuF_4$:$Yb_{0.2}Tm_{0.005}$@ $LiLuF_4$	yes	51 nm 28@11nm	QY 7.6	127 W/cm^2	Huang *et al.*[169]
$NaGdF_4$:$Yb_{0.22}Er_{0.025}$@$NaYF_4$ (heterogenous doping)	yes	21 nm 10.5@5nm	QY 0.47±0.05	50 W/cm^2	Li et al.[170]
$NaGdF_4$:$Yb_{0.22}Er_{0.025}$@$NaYF_4$ (homogenous doping)	yes	21 nm 10.5@5nm	QY 0.89±0.05	50 W/cm^2	Li et al.[170]
$NaYF_4$:$Yb_{0.2}$,$Er_{0.02}$@$NaYF_4$	yes	14 nm 8@3nm	QY 0.49±0.25	100 W/cm^2	Gargas et al.[23]

Table 2. Overview of absolute QY or CE measured using the integrating sphere method.

5.2.2 Strategies to enhance upconversion intensity

The brightness of UCL depends on the absorption probability of excitation light, the energy transfer efficiency from sensitizer to activator (in co-doped systems) and subsequently, the radiative emission efficiency of the activator. Impaired upconversion intensity can be due to down-converted emission, surface quenching (from bound organic moieties, surface defects, or phonons), cross-relaxation and further excitation[171]. These properties can be influenced using several strategies, including host lattice manipulation, energy transfer modulation, surface

passivation, surface plasmon coupling, broadband sensitization and photonic crystal engineering, as summarized in a recent review by Liu's group[172]. We will describe the latest results reported within these categories, applied to enhance UCL brightness.

Energy transfer modulation through host lattice manipulation

Host lattice manipulation can induce increased crystal field asymmetries around the emitting Ln, which increases the probability of ED transitions and luminescence emission. Direct demonstration of the influence of the crystal lattice properties on UC luminescence can be realized in-situ and real-time by using a physical approach. Hao *et al.* applied an external electric field to Yb/Er-doped $BaTiO_3$ thin films, which increased the distance between the positive Ti^{4+} and negative O^{2-} ions and therefore lowered the symmetry at the Er^{3+} ions (which substituted the Ti^{4+} ions in BTO, 5 mol% doping), resulting in increased green emission of more than 2.5 times[173]. Another clear demonstration of crystal host lattice influenced brightness was recently reported by Wisser et al[174]. By placing α- and β-phase $NaYF_4$:Yb/Er co-doped UCNPs in a diamond anvil cell they could be subjected to pressures as high as 25 GPa. The increasing pressure resulted in lattice compression and thus a reduced distance between the lanthanide ions, as well as altered crystal field symmetry. As α-particles have centrosymmetric geometry at atmospheric pressure, increasing the pressure results in increased asymmetry and therefore enhanced transition probability. Together with a reduced distance between lanthanide ions (as apparent by reduced lattice parameters) this resulted in up to two-fold enhancement of UCL brightness for α-$NaYF_4$:Yb/Er NPs at 2.1 GPa, corresponding to a 1% decrease in lattice constant. On the other hand, β-particles exhibited a substantial decrease in UCL as a dependency of induced pressure (e.g. UCL halved at 2.1 GPa). Since the ionic distances were also decreased for the β-particles, the authors attribute the decrease in UCL to an increase in pressure-induced lattice defects that enhance the non-radiative relaxation rates. It should be noted that the particle size in these two cases was different, 200 and 90 nm for α- and β-phase respectively, and they were immersed in silicone oil. In addition to changes in UCL, red-shifts (+ ~1.2 nm) and blue-shifts (- ~1nm) of emitting states were also observed, these were indicative of crystal field modification.

The above examples of physically manipulating lattice properties enable modulation of the UCL which can be reversible up to the damage threshold[173, 174], which is not applicable in the case of chemical host lattice manipulation. It can thus provide additional insights into brightness enhancements caused by nuanced crystal field asymmetries. These can subsequently be used as feedback for chemically changing the host. Chemical host lattice manipulation can be realized by tailoring the crystal lattices through doping with differently sized ions. A dopant that is smaller compared to the oxide or fluoride host lattices, for example Li^+, results in crystal lattice contraction while a relatively large ion will result in lattice expansion[172]. Li^+ doping has resulted in 1 to 2 orders of magnitude enhancement in upconversion luminescence[175, 176]. Alternatively, doping of transition-metal ions can also lead to increased upconversion luminescence, as the

large *d*-orbitals of transition metals lead to strengthening of the electron-phonon coupling of the lanthanides[172, 177].

A strategy that falls in both categories of host lattice manipulation and energy-transfer modulation is the previously mentioned novel approach of clustering the Yb-sensitizers in the KYb_2F_7 host matrix doped with 2 mol% Er^{3+}, which results in both colour tuning and upconversion enhancement[52, 178]. Usually, high-doping levels of Yb^{3+} result in concentration quenching: due to an increased energy-migration distance the probability of quenching by lattice or surface defects is enhanced. However, in this novel lattice design the energy transfer remains within the tetrad Yb-clusters which reduces the quenching probability, while the high concentration of Yb-ions increases the absorption cross section for 980 nm and enhances the energy-transfer between Yb^{3+} and Er^{3+} (see fig. 8). The back-energy transfer between Yb^{3+} and Er^{3+} results in increased 3- and 4-photon radiative emission processes resulting in increased red (3x higher) and blue (8x higher) emission.

Increasing activator concentration and power density

High concentrations of activator ions (i.e. 2 mol% for Er^{3+} and 0.2 mol% for Tm^{3+} ions) usually also lead to concentration quenching due to cross-relaxation between the dopants[75, 172, 179, 180]. Two recent studies have demonstrated that concentration quenching can be overcome by excitation in the high-power regime. The first study was published by our group and reveals a 70-fold increase in 802 nm UCL from Tm^{3+} ions at 8% doping concentration and 2.5 x 10^6 W/cm^2 excitation density[25]. Basically, with increasing excitation densities the number of Tm^{3+} ions in intermediate states starts to saturate ($^3F_4$ and $^3H_4$ states in Fig. 15a), inducing alternative energy loss channels involving higher states ($^1G_4$ and $^1D_2$ states) which progressively switch on until they are also saturated. Thus, a low doping concentration and high I_{ex} result in an increased emission from 4- and 5-photon processes and saturation of UCL[25, 181]. By increasing the Tm^{3+} content in the nanocrystals, the absorbed and transferred energy is distributed over more of the intermediate states and the emission from the $^3H_4$ level at 802 nm is substantially increased (Fig. 15b). The absolute CE and integrated UCL brightness also significantly increase for densely-doped nanocrystals (Fig. 15c). The reduced distance between sensitizer and activator ions, and the increased activator concentration, are the causes for this enhanced upconversion efficiency in the high-power excitation regime, where the activation rate dominates the quenching rate[25]. The second study by Gargas *et al.* was directed at minimizing the NP size, while maintaining enough UCL to enable detection[23]. In the high-power regime, their sub-10 nm densely-doped NPs (20% Yb^{3+}, 20% Er^{3+}) were an order of magnitude brighter as compared with conventionally doped-NPs (20% Yb^{3+}, 2% Er^{3+}) of the same size. They reason that for such small UCNPs the surface-related energy losses are substantial (the dark surface layer occupies >80% of the total volume) and it dominates the self-quenching by cross-relaxation. In addition, as we have shown, the decay rate of smaller particles (surface/volume ratio > 0.5, size < 12 nm) is dominated by the defect-related decay, as crystalline defects provide channels for nonradiative transitions[46]. At high excitation density, the availability of many activator sites is most important, as the sensitizers

saturate and the radiative relaxation rates of Er^{3+} are significantly slower than photon absorption rates in this regime. Thus, for small single-particle imaging under high I_{ex} the design strategy should be aimed at as high as possible emitter concentrations, without compromising nanocrystal structural integrity. Such high sensitivity lends itself for detection of rare biomarkers, for example in blood or urine samples as the high excitation density is less favourable for *in vivo* imaging. A microstructured suspended core optical-fibre dip sensor represents a promising platform technology for such applications[25].

.

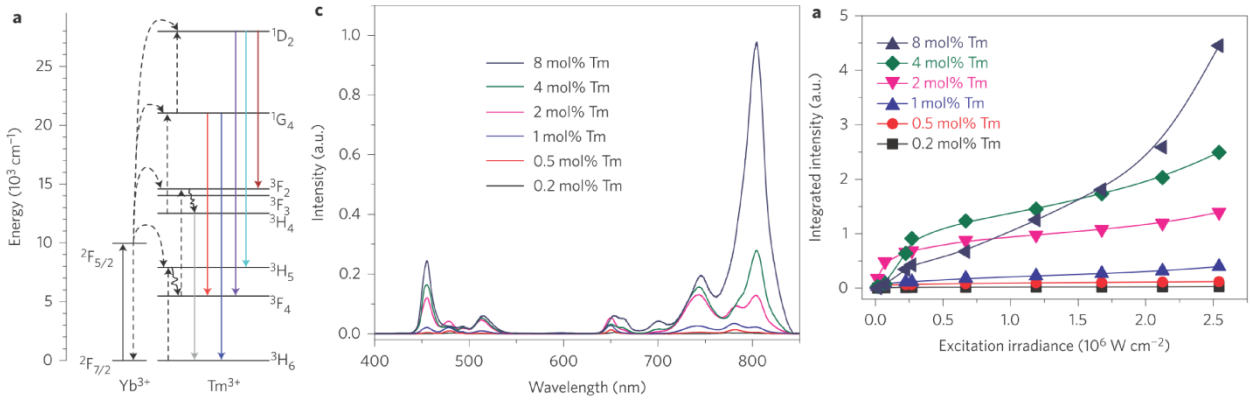

Fig. 15. Increasing the UCL by high doping concentrations of Tm^{3+} and high I_{ex} (a) Simplified energy-level diagram showing photon absorption/emission (solid arrows), energy transfer (dashed arrows) and multiphonon relaxation (curvy arrows) in Yb/Tm ions. (b) Emission spectra with increasing Tm^{3+} concentration in $NaYF_4$:Yb/Tm nanocrystals at high I_{ex} = 2.5 x 10^6 W/cm^2, show an increase in UCL especially for the 802 nm ($^3H_4 \rightarrow {}^3H_6$) peak. (c) Graph showing the importance of high I_{ex} for high Tm^{3+} concentration, to obtain the highest absolute UCL. Reprinted with permission from Zhao et al.[46]. Copyright 2013, Nature Publishing Group.

Core-shell strategies for surface passivation and geometric separation

As mentioned prevously, energy losses at the surface of NPs reduce their brightness. As the surface-to-volume ratio increases with decreasing size, the size of NPs is an important factor for UCL brightness as was discovered early on[11, 65], and later modelled by rate equations[176]. Furthermore, high-energy oscillators on the surface (surface impurities, ligands, solvent molecules) also induce non-radiative relaxation of the dopants close to the surface. An interesting recent study by Arppe *et al.* investigated on the effect of the vibrational modes of OH-groups in water by comparing the UCL intensity of bare and silanized NPs in H_2O and heavy water D_2O[182]. As expected, in Fig. 16 the intensity decreased in H_2O as compared with D_2O, and to a greater extent for the bare particles than the silica-shell particles. Further investigation on the decay times of the radiative transitions in Er^{3+} (via higher order excitation at 980 nm and direct excitation at 380 nm) and Yb^{3+} (via direct excitation at 930 nm) revealed that the Yb^{3+} relaxation rate increased much more in water than the Er^{3+} relaxation rates. Thus, this study exposes that the Yb ions interact more strongly with vibrational modes of water than the Er and Tm ions. Since Yb-Yb energy migration is efficient and it can travel long distances, a large crystal volume can effectively be quenched by the surface. Thus, surface passivation which prevents ion contact with the solvent by means of core-shell structures represents an important strategy for brightness

enhancement[183]. The shell may consist of the same crystal as the core (epitaxial shell); it can be built from other materials like polymers, non-crystalline silica, and carbon coating (nonepitaxial shell); or a combination of both. Usually, coating the UCNPs has other functions besides surface passivation, such as the inclusion of absorbing[50] or fluorescent dyes[184] for optical interactions, or the production of water-soluble NPs amenable to further surface modification for biological interactions[185]. Recently, a comprehensive review on the advantages, synthesis and applications of core-shell NPs was published by Prasad's group[186]. Here, we will mainly focus on the effects of core-shell strategy on brightness enhancement through the suppression of surface quenching and cross-relaxation processes.

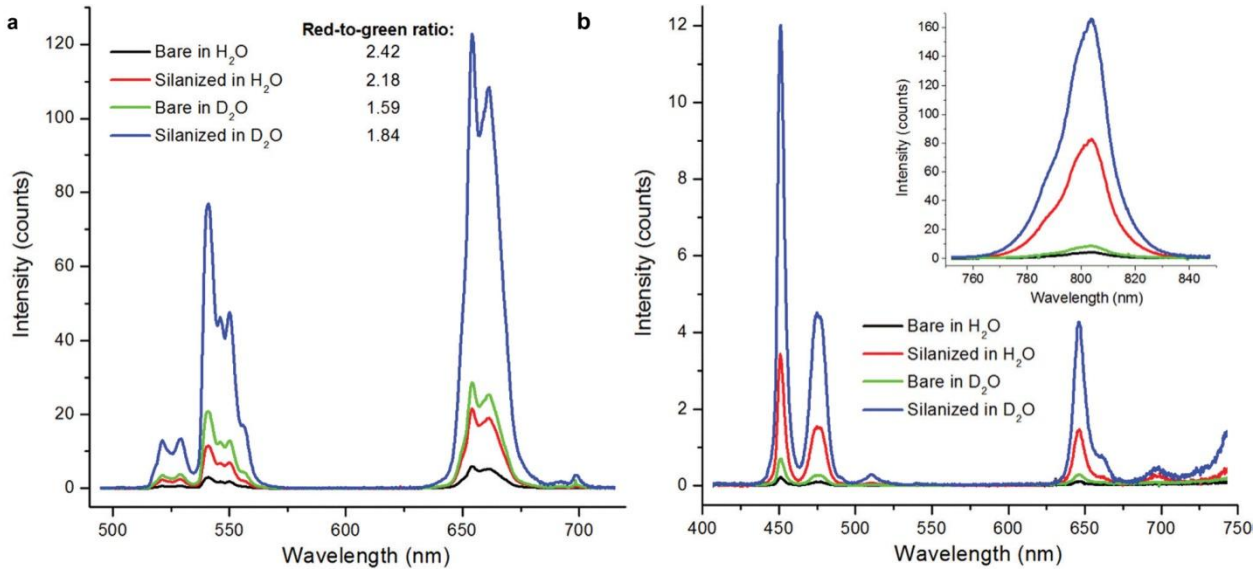

Fig. 16. By measuring the UCL in H_2O and D_2O the effects of surface quenching by OH-groups can be quantified as shown in (a) for $NaYF_4$:Yb,Er UCNPs and in (b) for $NaYF_4$:Yb,Tm UCNPs, both bare and silanized. Reproduced from Arppe et al. ref.[182] with permission from The Royal Society of Chemistry.

Surface quenching can occur when excited Ln^{3+} ions are located close to the UCNP surface, either via local absorption and energy transfer processes, or through energy migration from the core. Thus, increasing the distance from the surface by coating the particle with an inert epitaxial or non-epitaxial shell will reduce this loss, with a trade-off of a larger particle size. The addition of a shell can increase UCL by orders of magnitude, for example 450 times by the addition of a ~7 nm CaF_2 shell[147] and 10^4 times by the addition of a ~10 nm $NaYF_4$ shell[187], both to small (~10 nm) particles. The absolute quantum yields of these particles are still below 1.5%. The extraordinary enhancements also suggest a large difference in imperfections in the core particles, and the ability of the different core types to passivate these imperfections and minimize surface quenching[183]. For larger 28 nm core particles, the UCL increased 10 – 100 times upon the addition of a 11 nm $LiLuF_4$ shell. These $LiLuF_4$:$Yb_{0.2}Er_{0.01}$@$LiLuF_4$ and $LiLuF_4$:$Yb_{0.2}Tm_{0.005}$@$LiLuF_4$ NCs exhibited absolute quantum yields of 5.0% and 7.6% respectively[169]. The brightness increase with shell thickness has also been studied, with authors coming to different conclusions. Gargas *et al.* find that the UCL increases with shell thickness but

saturates above 1.8 nm thickness[23], while other studies find optimum thicknesses of ~2.4 – 3 nm or 6 nm[183, 186]. Recently, Chen and Huang showed that the core size and the ratio of shell precursors to core size in the reaction, impact on the completeness of the epitaxial shell covering the core and resulting morphology of the nanocrystals[187]. As incomplete core-shell structures will also give rise to enhanced UCL, this could clarify the variable outcomes of UCL increase in core-shell UCNPs[171].

As described in Section 3.2, energy transfer can result in desired ETU, energy migration or phonon-assisted energy migration, but also in the undesired cross-relaxation. Cross-relaxation can be reduced by spatially separating the dopant ions by the core-shell strategy, which is achieved by adding a so-called active shell doped with activators or sensitizers. The active shell can be used to enhance harvesting of excitation light by increasing the concentration of sensitizers, as was shown first for $NaGdF_4$:Er,Yb(2:20 mol%)@$NaGdF_4$:Yb(20 mol%) UCNPs that were significantly brighter compared to inert-shell and core-only particles[51]. In more recent designs, alternative sensitizers were doped in the shell. Xie *et al.* designed NCs with an active Nd-doped (20 mol%) $NaYF_4$ shell (~ 5 nm), and found that Nd^{3+} sensitizers are less susceptible to surface quenching compared to Yb^{3+} [156]. Importantly, the $NaYF_4$ (~ 30 nm) core was doped with Yb^{3+} ions (30 mol%) to accept and efficiently migrate the absorbed energy by Nd^{3+} to the activator ions Tm^{3+}(0.5 mol%), Er^{3+} (0.5%) or Ho^{3+} (1 mol%). Although the Nd-sensitized UCNPs usually exhibit reduced UCL compared to Yb-sensitized counterparts, the current design resulted in equal performance, while having the additional biomedical advantage to be excited at around 800 nm where tissue absorption is low. Recently, Huang amended this design by adding Yb^{3+} ions together with Nd^{3+} ions in the 3 nm shell (5 mol% respectively 30 mol%), coating the 20.6 nm $NaYF_4$:Nd,Yb,Ho(1:19:0.5 mol%) cores[188]. By codoping the shell with Yb^{3+} the UCL increased another 2.5 times. The overall UCL enhancement as compared to core-only UCNPs was 405 times for the Nd-doped shell[156] and 990 times for the Nd/Yb-doped shell[188], although the comparison seems unfair due to the much smaller number of sensitizers in the core-only UCNPs. However, increasing the number of sensitizers in the core-only NPs would induce concentration quenching and reduction of UCL. In this case the shell functions to suppress surface and concentration quenching and increase the absorption of excitation light, all leading to enhanced UCL. An important remark here is that the particles have not been tested in aqueous solutions able to efficiently quench the Yb^{3+} excited state, as previously described[182].

Recently, more advanced UCNP structures have been designed, such as UCNPs with homogeneous doping throughout the core by successive layer-by-layer synthesis[170], or the addition of multiple functional shells. The shells can for example serve as energy migration buffers from the sensitizing and accumulating core to the outer activator-doped shells[54], ultimately coated with an inert shell to reduce surface quenching[55]. In another application to increase the efficiency of solar cells, UCNPs with multiple individual shells containing different types of activators were synthesized with an inert $NaYF_4$ layer in between each shell: $NaYF_4$:Er(10mol%)@$NaYF_4$@ $NaYF_4$:Ho(10mol%)@$NaYF_4$@ $NaYF_4$:Tm(1mol%)@$NaYF_4$,

see Fig. 17[189]. This prevented cross-relaxation between different types of dopants. The resulting particles could absorb a broad spectrum in the IR (Ho^{3+}: 1120-1190 nm, Tm^{3+}: 1190 – 1260 nm and Er^{3+}: 1450-1580 nm) and emit efficiently in the VIS/NIR, about 1 order of magnitude brighter as compared to a single core@inert shell particle containing the same amounts of dopants. The utilization of different types of Ln^{3+} able to function as sensitizers (like Yb^{3+}, Nd^{3+}, Er^{3+} and Ho^{3+}) thus additionally results in broadband spectral sensitizing of NIR light, and can enhance UCL brightness.

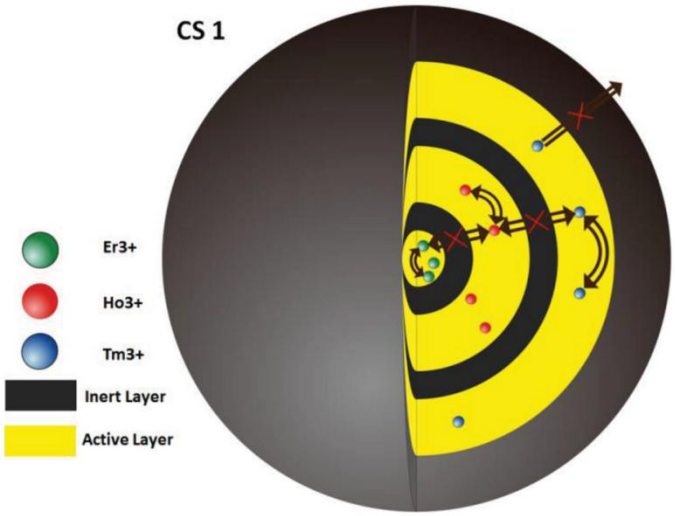

Fig. 17. Multilayered design with inert sub-layers to reduce cross-relaxation between activators: $NaYF_4$:Er(10mol%)@$NaYF_4$@$NaYF_4$:Ho(10mol%)@$NaYF_4$@$NaYF_4$:Tm(1mol%)@$NaYF_4$. Reprinted with permission from Shao et al[189]. Copyright 2014, Wiley-VCH Verlag GmbH & Co. KGaA.

Plasmonic enhancement and other external resonators

Upconversion brightness can also be increased by external effects, such as enhanced electromagnetic fields. Confined free electrons on the surface of noble metal nanomaterials can oscillate with an incoming optical field, which is largely enhanced at resonance frequencies. If the resonant frequencies of these surface plasmons are coupled to the UCNPs, they can influence the the decay rates, absorption cross section and energy transfer coefficients of the Ln ions. The surface plasmon resonant frequencies can be influenced by the size and shape of the noble metal nanomaterials. As derived by Park *et al.* in a recent review on plasmon enhancement in upconversion, the plasmon enhancement factor *F* for UCNPs is mainly proportional to the transfer rate from sensitizer to activator (F_{d4}), the square of the absorption enhancement factor (F_a) and inversely proportional to the square of the sensitizer decay rate (F_{D10}), in the weak excitation limit[53, 120]:

$$F_{weak} \approx \frac{F_{d4}F_a^2}{F_{D10}^2}. \quad (32)$$

In the strong excitation limit, the enhancement factor is simply:

$$F_{strong} \approx F_{a,} \quad (33)$$

because all other processes leading to UC are saturated. The absorption enhancement factor F_a is proportional to the absorption cross section, which in turn is proportional to the square of the plasmon-enhanced external electric field: $|E_{loc}/E_0|^2$, where E_{loc} and E_0 are the local electric field and the incident electric field respectively. Since the UC intensity proportional to the n-th power of the excitation light irradiance (n>1)[100] plasmonic enhancement is particularly strong near the excitation wavelength of UCL. Moreover, the rate of energy transfer between sensitizers and activators can also be increased by surface plasmons. It has been shown that this enhancement factor depends on the relationship between the plasmon energy and the energy mismatch of the levels involved in energy transfer. It also depends on the distance from the plasmonic surface and the separation between sensitizer and activator[53]. Finally, surface plasmons can increase the number of photon states due to the large increase in local photon density, and thereby the radiative decay rates. The enhancement of radiative decay rates is measured by the Purcell factor, named after the first pioneer in this area[190]. The presence of metal can also quench the UC by offering additional non-radiative decay channels. Together with the Purcell effect, these enhance the unwanted sensitizer decay rate $F_{D10.}$ At a certain distance close to the surface the quenching effect dominates the electric-field enhancement effect on F_a and F_{d4}. Therefore, there is always an optimal spacing between plasmonic nanostructures and the upconverting ions where plasmonic enhancement is maximal[53, 191, 192]. From Eqn. (32) and its explanation, it is obvious that choosing the plasmon frequency close to the excitation frequency will induce the largest enhancement effect, especially in the low excitation regime. The enhancement of the energy transfer rate is limited, as it is generally already high due to small ion-ion separations[53]. In Fig. 18 a literature overview is given on the achieved enhancement factors using surface plasmons from gold and silver, in different geometries.

Obviously, the size and geometry of the UCNP-plasmonic hybrid structure has a large influence on the applicability. For biomedical applications the favourable small size is achievable by using core-shell architecture where the metallic nanostructure can form the core or the shell of the UCNPs, often with a silica layer to optimize the spacing[183]. In 2011, we reported the synthesis of gold-shell coated $NaYF_4$:Er,Yb@SiO_2 nanoparticles, with enhancement factors of ~9.1 and ~6.7 for green and red emission respectively, due to plasmon-enhanced absorption at 980 nm[193]. Recently, it was shown that the combination of gold nanorods and UCNPs deposited on thin films can function as a plasmon-enhanced nanothermometric structure[194]. Gold nanorods showed collective heating upon surface plasmon activation, which in turn tuned the green-to-red emission ratio of the UCNPs. Though the current geometry is not compatible with *in vivo* delivery, future designs of gold-UCNP hybrid structures can potentially be used for photothermal therapy, while the UCNP emission can be utilized to monitor the actual temperatures. With applications in solar technology, Lee *et al.* recently created a plasmonic nanostructure based on a metal nanodisk-insulator-metal design with plasmon resonance frequencies in both the excitation and emission wavelengths of Er^{3+}, resulting in a UCL enhancement factor of 174 times[97]. They also included a layer consisting of Tb^{3+} ions for downconversion (UV absorption to VIS emission), and calculated the downconversion enhancement factor to be 29-fold. This structure is thus very

efficient for enhancing visible luminescence from UV and NIR to match the optimal spectral responsivity of solar cells.

Other external materials such as photonic-crystals and resonant waveguides can also cause an enhancement of local electric field intensity and enhanced density of optical states[172, 195]. The highest enhancement factor reported to date was published this year by Lin *et al.*[196]. They constructed a resonant waveguide grating structure, in which 30 nm $NaYF_4$:Yb,Tm (20:2mol%) nanocrystals were embedded in the top cladding layer. Matching the excitation and emission wavelength to the guided-mode resonance of the structure resulted in very high UCL enhancement of blue and red light, by a factor of up to 10^4 in case of excitation resonance, and an additional factor 3 for the case of emission (or 'extraction') resonance. This extreme enhancement is in part due to the 3- and 4-photon UC processes in Tm^{3+}, resulting in higher-order enhancement in a strongly enhanced local-field at the excitation wavelength.

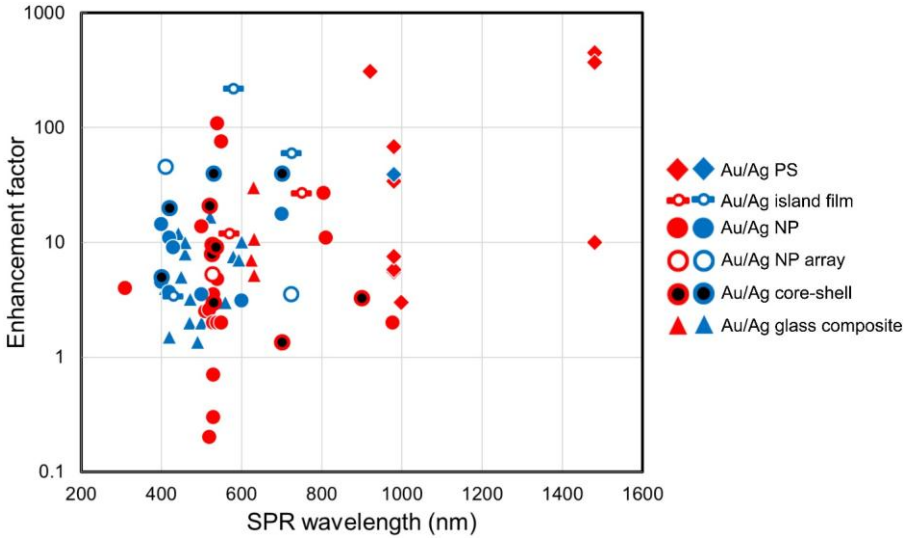

Fig. 18 Overview of literature reports of the enhancement factor for UCL as function of surface plasmon resonance (SPR) wavelength and for various geometries utilizing gold and silver, represented by red and blue symbols, respectively. NP – nanoparticle, PS – patterned structure. Reproduced from Park et al.[53] with permission from The Royal Society of Chemistry.

Optimizing the QY/CE through varying excitation schemes

Generally, increasing the excitation density results in an increased UCL brightness. For biomedical applications, the excitation density and therefore the QY/CE are limited by safety standards for radiation exposure (ANSI). The maximum permissible exposure for pulsed excitation is higher as compared with CW excitation, due to the ability of tissue to dissipate heat during excitation. By utilizing these rules and analyzing the time-resolved rate equations while changing the pulse parameters (pulse width, repetition rate, and peak power) it was shown that a higher CE can be accomplished using pulsed excitation schemes while maintaining the same average power density[118]. The modelling showed that it is important to choose the excitation parameters to ensure a sufficiently long pulse width while keeping the energy transfer transitions non-saturated. For example, a CE-gain factor of 8 was obtained for a 20 ms pulse at 25 W/cm^2 in

a 2 Hz repetition rate, as compared with the equivalent CE under CW excitation with excitation power density of 0.12 W/cm^2.

6. Summary and Outlook

This review provides a guide to the understanding of the fundamental photophysical processes leading to upconversion luminescence, discusses practical rate equation approaches to quantitatively interrogate them, and provides an overview of experimental strategies to influence, control and optimize the optical properties of upconversion at nanoscale. Given the volume and scope of theoretical and experimental research articles recently published, the progress in the field is expected to rapidly increase. We note that it is important to find key application niches for UCNPs in various fields, by keeping a realistic view on their optical properties and practical synthesis methods. For example, the large dependency of brightness on host lattice defects dictates the need for high quality and predictable synthesis chemistry[46, 127]. Another important remark is the need to assess the nanotoxicity, not only for use in biomedical applications, but also regarding the fate of nanoparticles in laboratory waste[197, 198]. Potential toxicity may result not only from the chemical composition, but also from the small size of UCNPs, enabling them to bypass biological barriers and/or accumulate in the tissue[197].

At the same time, the increasing information on the optimization of the photophysical processes in UCNPs will enhance their quality and applications in many fields[12]. One aspect not highlighted in this review is the application and control of the UCL lifetime. Using the lifetime feature extends the functionality of UCNPs towards lifetime multiplexing applications for the simultaneous detection of a large number of biomarkers, and towards new strategies for data storage and security measures[199]. Strategies to influence the UCL lifetime[46, 199, 200] are likely to be intensely investigated in the future.

Increasing the absorption efficiency and refining the energy transfer within UCNPs are two key directions of current research, aimed at enhancement of the desired optical properties. The combinations of recent successes, such as high concentration of clustered Yb-sensitizers[52] and enhancement by external resonance structures[53, 196] may prove to be instrumental to further advancement, and pave the way to groundbreaking interdisciplinary applications of this exciting class of nanoparticles.

Author contributions:
A. Nadort made the major contributions to the optical properties section and the preparation of the manuscript. J. Zhao made major contributions to the photophysics sections and fundamentals and review structure and scope of the review, and E.M. Goldys contributed to the theory and final form of manuscript.

Acknowledgements:

This work was partially funded by the Australian Research Council (CE14010003 and DP140104458 to E.G.). We thank Dr Yiqing Lu and Dr. Helen Pask for drawing our attention to selected literature references.

References

1. F. E. Auzel, *Proceedings of the IEEE*, 1973, **61**, 758-786.
2. J. Midwinter and J. Warner, *Journal of Applied Physics*, 1967, **38**, 519-523.
3. C. Piguet, *Nature chemistry*, 2014, **6**, 370-370.
4. P. Hardman, W. Clarkson, G. Friel, M. Pollnau and D. Hanna, *Quantum Electronics, IEEE Journal of*, 1999, **35**, 647-655.
5. S. Grubb, K. Bennett, R. Cannon and W. Humer, *Electronics Letters*, 1992, **28**, 1243-1244.
6. R. Scheps, *Progress in Quantum Electronics*, 1996, **20**, 271-358.
7. A. Oliveira, M. De Araujo, A. Gouveia-Neto, A. Sombra, J. M. Neto and N. Aranha, *Journal of applied physics*, 1998, **83**, 604-606.
8. D. Yeh, W. Sibley and M. Suscavage, *Journal of applied physics*, 1988, **63**, 4644-4650.
9. A. Bril, J. Sommerdijk and A. De Jager, *Journal of The Electrochemical Society*, 1975, **122**, 660-663.
10. S. Heer, K. Kömpe, H. U. Güdel and M. Haase, *Advanced Materials*, 2004, **16**, 2102-2105.
11. G. Yi, H. Lu, S. Zhao, Y. Ge, W. Yang, D. Chen and L.-H. Guo, *Nano Letters*, 2004, **4**, 2191-2196.
12. J. Zhou, Q. Liu, W. Feng, Y. Sun and F. Li, *Chemical reviews*, 2014.
13. F. Wang and X. Liu, *Chemical Society Reviews*, 2009, **38**, 976-989.
14. P. Qiu, N. Zhou, H. Chen, C. Zhang, G. Gao and D. Cui, *Nanoscale*, 2013, **5**, 11512-11525.
15. G. Chen, H. Qiu, P. N. Prasad and X. Chen, *Chemical reviews*, 2014, **114**, 5161-5214.
16. D. Yang, Z. Hou, Z. Cheng, C. Li and J. Lin, *Chemical Society Reviews*, 2015, **44**, 1416-1448.
17. G. Liu, *Chemical Society Reviews*, 2015.
18. X. Liu, R. Deng, Y. Zhang, Y. Wang, H. Chang, L. Huang and X. Liu, *Chemical Society Reviews*, 2015, **44**, 1479-1508.
19. J.-C. G. Bünzli, *Journal of Coordination Chemistry*, 2014, **67**, 3706-3733.
20. B. E. Cohen, *Nature*, 2010, **467**, 407-408.
21. W. Denk, J. H. Strickler and W. W. Webb, *Science*, 1990, **248**, 73-76.
22. M. Nuriya, J. Jiang, B. Nemet, K. B. Eisenthal and R. Yuste, *Proceedings of the National Academy of Sciences of the United States of America*, 2006, **103**, 786-790.
23. D. J. Gargas, E. M. Chan, A. D. Ostrowski, S. Aloni, M. V. P. Altoe, E. S. Barnard, B. Sanii, J. J. Urban, D. J. Milliron and B. E. Cohen, *Nature nanotechnology*, 2014, **9**, 300-305.
24. A. Gnach and A. Bednarkiewicz, *Nano Today*, 2012, **7**, 532-563.
25. J. Zhao, D. Jin, E. P. Schartner, Y. Lu, Y. Liu, A. V. Zvyagin, L. Zhang, J. M. Dawes, P. Xi and J. A. Piper, *Nature nanotechnology*, 2013, **8**, 729-734.
26. M. Illemassene, N. Edelstein, K. Murdoch, M. Karbowiak, R. Cavellec and S. Hubert, *Journal of luminescence*, 2000, **86**, 45-60.
27. J. Suyver, A. Aebischer, D. Biner, P. Gerner, J. Grimm, S. Heer, K. Krämer, C. Reinhard and H. Güdel, *Optical Materials*, 2005, **27**, 1111-1130.
28. S. V. Eliseeva and J.-C. G. Bünzli, *Chemical Society Reviews*, 2010, **39**, 189-227.
29. J.-C. G. Bünzli, *Chemical reviews*, 2010, **110**, 2729-2755.
30. F. Auzel, *Chemical reviews*, 2004, **104**, 139-174.
31. H. Russell and F. Saunders, *astrophysical journal* 1925, **61**, 38.
32. F. Auzel, *Comptes Rendus Hebdomadaires Des Seances De L Academie Des Sciences Serie B*, 1966, **262**, 1016-&.

33. J. v. Vleck, *Journal of physical chemistry*, 1937, **41**, 67-80.
34. J. Suyver, J. Grimm, K. Krämer and H. Güdel, *Journal of Luminescence*, 2005, **114**, 53-59.
35. J. Suyver, J. Grimm, M. Van Veen, D. Biner, K. Krämer and H. Güdel, *Journal of Luminescence*, 2006, **117**, 1-12.
36. A. Patra, C. S. Friend, R. Kapoor and P. N. Prasad, *Applied physics letters*, 2003, **83**, 284-286.
37. T. Hahn, *International tables for crystallography: Brief teaching edition of volume A, Space-group symmetry*, Springer Netherlands, 1993.
38. G. Liu and B. Jacquier, *Spectroscopic properties of rare earths in optical materials*, Springer Science & Business Media, 2006.
39. D. R. Gamelin and H. U. Güdel, *The Journal of Physical Chemistry B*, 2000, **104**, 10222-10234.
40. S. Lüthi, M. Hehlen, T. Riedener and H. Güdel, *Journal of luminescence*, 1998, **76**, 447-450.
41. J. L. Sommerdijk and A. Bril, *Philips technical review*, 1974, **34**, 24-32.
42. E. M. Chan, G. Han, J. D. Goldberg, D. J. Gargas, A. D. Ostrowski, P. J. Schuck, B. E. Cohen and D. J. Milliron, *Nano Letters*, 2012, **12**, 3839-3845.
43. J. Liu, H. Deng, Z. Huang, Y. Zhang, D. Chen and Y. Shao, *Physical Chemistry Chemical Physics*, 2015.
44. F. Wang and X. Liu, *Journal of the American Chemical Society*, 2008, **130**, 5642-5643.
45. F. Wang, Y. Han, C. S. Lim, Y. Lu, J. Wang, J. Xu, H. Chen, C. Zhang, M. Hong and X. Liu, *Nature*, 2010, **463**, 1061-1065.
46. J. Zhao, Z. Lu, Y. Yin, C. McRae, J. A. Piper, J. M. Dawes, D. Jin and E. M. Goldys, *Nanoscale*, 2013, **5**, 944-952.
47. R. Deng, F. Qin, R. Chen, W. Huang, M. Hong and X. Liu, *Nature nanotechnology*, 2015.
48. C. Zhang, L. Yang, J. Zhao, B. Liu, M. Y. Han and Z. Zhang, *Angewandte Chemie*, 2015, **127**, 11693-11697.
49. Z. Li, Y. Zhang and S. Jiang, *Advanced Materials*, 2008, **20**, 4765-4769.
50. L. Zhou, R. Wang, C. Yao, X. Li, C. Wang, X. Zhang, C. Xu, A. Zeng, D. Zhao and F. Zhang, *Nature communications*, 2015, **6**.
51. F. Vetrone, R. Naccache, V. Mahalingam, C. G. Morgan and J. A. Capobianco, *Advanced Functional Materials*, 2009, **19**, 2924-2929.
52. J. Wang, R. Deng, M. A. MacDonald, B. Chen, J. Yuan, F. Wang, D. Chi, T. S. A. Hor, P. Zhang and G. Liu, *Nature materials*, 2014, **13**, 157-162.
53. W. Park, D. Lu and S. Ahn, *Chemical Society Reviews*, 2015, **44**, 2940-2962.
54. F. Wang, R. Deng, J. Wang, Q. Wang, Y. Han, H. Zhu, X. Chen and X. Liu, *Nature Materials*, 2011, **10**, 968-973.
55. Q. Su, S. Han, X. Xie, H. Zhu, H. Chen, C.-K. Chen, R.-S. Liu, X. Chen, F. Wang and X. Liu, *Journal of the American Chemical Society*, 2012, **134**, 20849-20857.
56. W. Carnall, H. Crosswhite and H. Crosswhite, *Energy Level Structure and Transition Probabilities of the Trivalent Lanthanides in LaF-3*, 1978.
57. D. McCumber, *Physical Review*, 1964, **136**, A954.
58. E. Merzbacher, *Quantum Mechanics*, J. Wiley, NY, USA, 1998.
59. B. Judd, *Physical Review*, 1962, **127**, 750.
60. G. Ofelt, *The Journal of Chemical Physics*, 1962, **37**, 511-520.
61. C. Peng, H. Zhang, J. Yu, Q. Meng, L. Fu, H. Li, L. Sun and X. Guo, *The Journal of Physical Chemistry B*, 2005, **109**, 15278-15287.
62. O. Malta, M. C. dos Santos, L. Thompson and N. Ito, *Journal of luminescence*, 1996, **69**, 77-84.
63. O. Malta, H. Brito, J. Menezes, F. G. e Silva, S. Alves, F. Farias and A. De Andrade, *Journal of luminescence*, 1997, **75**, 255-268.

64. E. E. Teotonio, J. G. Espínola, H. F. Brito, O. L. Malta, S. F. Oliveira, D. L. de Faria and C. M. Izumi, *Polyhedron*, 2002, **21**, 1837-1844.
65. J. Boyer, F. Vetrone, J. Capobianco, A. Speghini and M. Bettinelli, *The Journal of Physical Chemistry B*, 2004, **108**, 20137-20143.
66. G. De Sa, O. Malta, C. de Mello Donegá, A. Simas, R. Longo, P. Santa-Cruz and E. Da Silva, *Coordination Chemistry Reviews*, 2000, **196**, 165-195.
67. C. A. Kodaira, H. F. Brito and M. C. F. Felinto, *Journal of Solid State Chemistry*, 2003, **171**, 401-407.
68. P. F. Moulton, *JOSA B*, 1986, **3**, 125-133.
69. A. Kaminskii, *Crystalline lasers: physical processes and operating schemes*, CRC press, 1996.
70. B. M. Walsh, *Judd-Ofelt theory: principles and practices*, Springer, 2006.
71. E. M. Chan, D. J. Gargas, P. J. Schuck and D. J. Milliron, *The Journal of Physical Chemistry B*, 2012, **116**, 10561-10570.
72. D. L. Dexter, *The Journal of Chemical Physics*, 1953, **21**, 836-850.
73. T. Förster, *Annalen der physik*, 1948, **437**, 55-75.
74. S. Fischer, B. Fröhlich, K. W. Kramer and J.-C. Goldschmidt, *The Journal of Physical Chemistry C*, 2014.
75. K. W. Krämer, D. Biner, G. Frei, H. U. Güdel, M. P. Hehlen and S. R. Lüthi, *Chemistry of Materials*, 2004, **16**, 1244-1251.
76. M. Inokuti and F. Hirayama, *The journal of chemical physics*, 1965, **43**, 1978-1989.
77. J. Ganem, J. Crawford, P. Schmidt, N. Jenkins and S. Bowman, *Physical Review B*, 2002, **66**, 245101.
78. J. Collins, *ECS Journal of Solid State Science and Technology*, 2016, **5**, R3170-R3184.
79. S. Schietinger, L. d. S. Menezes, B. r. Lauritzen and O. Benson, *Nano letters*, 2009, **9**, 2477-2481.
80. G. Liu, H. Zhuang and X. Chen, *Nano Letters*, 2002, **2**, 535-539.
81. A. G. Macedo, R. A. Ferreira, D. Ananias, M. S. Reis, V. S. Amaral, L. D. Carlos and J. Rocha, *Advanced Functional Materials*, 2010, **20**, 624-634.
82. A. M. Kelley, *ACS nano*, 2011, **5**, 5254-5262.
83. F. Pandozzi, F. Vetrone, J.-C. Boyer, R. Naccache, J. A. Capobianco, A. Speghini and M. Bettinelli, *The Journal of Physical Chemistry B*, 2005, **109**, 17400-17405.
84. N. Yamada, S. Shionoya and T. Kushida, *Journal of the Physical Society of Japan*, 1972, **32**, 1577-1586.
85. T. Miyakawa and D. Dexter, *Physical Review B*, 1970, **1**, 2961.
86. Z. Wang, S. Zeng, J. Yu, X. Ji, H. Zeng, S. Xin, Y. Wang and L. Sun, *Nanoscale*, 2015, **7**, 9552-9557.
87. B. Masenelli, O. Mollet, O. Boisron, B. Canut, G. Ledoux, J.-M. Bluet, P. Mélinon, C. Dujardin and S. Huant, *Nanotechnology*, 2013, **24**, 165703.
88. F. Wang, J. Wang and X. Liu, *Angewandte Chemie*, 2010, **122**, 7618-7622.
89. J. R. Lakowicz, 2006.
90. L. Gomes, L. Courrol, L. Tarelho and I. Ranieri, *Physical review B*, 1996, **54**, 3825.
91. O. Igoshin and A. Burshtein, *Journal of luminescence*, 2000, **92**, 123-132.
92. W. Naumann, *The Journal of chemical physics*, 1999, **111**, 2414-2422.
93. A. Popov, V. Gladkikh and A. Burshtein, *The Journal of Physical Chemistry A*, 2003, **107**, 8177-8183.
94. W. L. Barnes, R. Laming, E. J. Tarbox and P. Morkel, *Quantum Electronics, IEEE Journal of*, 1991, **27**, 1004-1010.
95. V. Singh, V. Rai, I. Ledoux-Rak, L. Badie and H.-Y. Kwak, *Applied Physics B*, 2009, **97**, 805-809.
96. M. Ding, D. Chen, Z. Wan, Y. Zhou, J. Zhong, J. Xi and Z. Ji, *Journal of Materials Chemistry C*, 2015, **3**, 5372-5376.

97. K.-T. Lee, J.-H. Park, S. J. Kwon, H.-K. Kwon, J. Kyhm, K.-W. Kwak, H. S. Jang, S. Y. Kim, J. S. Han and S.-H. Lee, *Nano letters*, 2015, **15**, 2491-2497.
98. X. F. Yu, L. D. Chen, M. Li, M. Y. Xie, L. Zhou, Y. Li and Q. Q. Wang, *Advanced Materials*, 2008, **20**, 4118-4123.
99. M.-Y. Xie, L. Yu, H. He and X.-F. Yu, *Journal of Solid State Chemistry*, 2009, **182**, 597-601.
100. M. Pollnau, D. Gamelin, S. Lüthi, H. Güdel and M. Hehlen, *Physical Review B*, 2000, **61**, 3337.
101. D. Khoptyar, S. Sergeyev and B. Jaskorzynska, *Quantum Electronics, IEEE Journal of*, 2005, **41**, 205-212.
102. D. Khoptyar and B. Jaskorzynska, *JOSA B*, 2005, **22**, 2091-2098.
103. S. Sergeyev and B. Jaskorzynska, *Physical Review B*, 2000, **62**, 15628.
104. J. L. Philipsen and A. Bjarklev, *Quantum Electronics, IEEE Journal of*, 1997, **33**, 845-854.
105. S. Bjurshagen, J. E. Hellström, V. Pasiskevicius, M. C. Pujol, M. Aguiló and F. Díaz, *Applied optics*, 2006, **45**, 4715-4725.
106. E. Cantelar and F. Cusso, *Applied Physics B*, 1999, **69**, 29-33.
107. P. A. Burns, J. M. Dawes, P. Dekker, J. A. Piper, H. Jiang and J. Wang, *IEEE J. Quantum Electron.*, 2004, **40**, 1575-1582.
108. C. Li, C. Wyon and R. Moncorge, *Quantum Electronics, IEEE Journal of*, 1992, **28**, 1209-1221.
109. W. Wang, M. Wu and G. Liu, *Spectroscopy Letters*, 2007, **40**, 259-269.
110. N. Bogdan, F. Vetrone, G. A. Ozin and J. A. Capobianco, *Nano letters*, 2011, **11**, 835-840.
111. F. Auzel, *Journal of Luminescence*, 1984, **31**, 759-761.
112. J.-C. Boyer and F. C. Van Veggel, *Nanoscale*, 2010, **2**, 1417-1419.
113. Q. Lü, F. Guo, L. Sun, A. Li and L. Zhao, *The Journal of Physical Chemistry C*, 2008, **112**, 2836-2844.
114. S. Huang, S. T. Lai, L. Lou, W. Jia and W. Yen, *Physical Review B*, 1981, **24**, 59.
115. G. Qin, S. Huang, Y. Feng, A. Shirakawa, M. Musha and K.-I. Ueda, *Applied Physics B*, 2006, **82**, 65-70.
116. F. Ostermayer Jr, J. Van der Ziel, H. Marcos, L. Van Uitert and J. Geusic, *Physical Review B*, 1971, **3**, 2698.
117. Z. Liang, Y. Cui, S. Zhao, L. Tian, J. Zhang and Z. Xu, *Journal of Alloys and Compounds*, 2014, **610**, 432-437.
118. H. Liu, C. T. Xu, G. Dumlupinar, O. B. Jensen, P. E. Andersen and S. Andersson-Engels, *Nanoscale*, 2013, **5**, 10034-10040.
119. R. H. Page, K. I. Schaffers, P. A. Waide, J. B. Tassano, S. A. Payne, W. F. Krupke and W. K. Bischel, *JOSA B*, 1998, **15**, 996-1008.
120. D. Lu, S. K. Cho, S. Ahn, L. Brun, C. J. Summers and W. Park, *ACS nano*, 2014, **8**, 7780-7792.
121. R. Martín-Rodríguez, F. T. Rabouw, M. Trevisani, M. Bettinelli and A. Meijerink, *Advanced Optical Materials*, 2015, **3**, 558-567.
122. U. Skrzypczak, G. Seifert and S. Schweizer, *Advanced Optical Materials*, 2015, **3**, 541-545.
123. U. Skrzypczak, C. Pfau, G. Seifert and S. Schweizer, *The Journal of Physical Chemistry C*, 2014, **118**, 13087-13098.
124. R. B. Anderson, S. J. Smith, P. S. May and M. T. Berry, *The Journal of Physical Chemistry Letters*, 2013, **5**, 36-42.
125. P. Villanueva-Delgado, K. W. Krämer and R. Valiente, *The Journal of Physical Chemistry C*, 2015, **119**, 23648-23657.
126. S. Fischer, F. Hallermann, T. Eichelkraut, G. von Plessen, K. W. Krämer, D. Biner, H. Steinkemper, M. Hermle and J. C. Goldschmidt, *Optics express*, 2012, **20**, 271-282.
127. E. M. Chan, *Chemical Society Reviews*, 2015, **44**, 1653-1679.
128. B. Peng and T. Izumitani, *Optical Materials*, 1995, **4**, 701-711.

129. A. Braud, S. Girard, J. Doualan, M. Thuau, R. Moncorgé and A. Tkachuk, *Physical Review B*, 2000, **61**, 5280.
130. E. M. Chan, E. S. Levy and B. E. Cohen, *Advanced Materials*, 2015.
131. S. Sivakumar, F. C. M. van Veggel and M. Raudsepp, *Journal of the American Chemical Society*, 2005, **127**, 12464-12465.
132. M. Bettinelli, *Nature nanotechnology*, 2015, **10**, 203-204.
133. J. M. Meruga, A. Baride, W. Cross, J. J. Kellar and P. S. May, *Journal of Materials Chemistry C*, 2014, **2**, 2221-2227.
134. V. Mahalingam, F. Vetrone, R. Naccache, A. Speghini and J. A. Capobianco, *Advanced Materials*, 2009, **21**, 4025-4028.
135. S. Ye, G. Chen, W. Shao, J. Qu and P. N. Prasad, *Nanoscale*, 2015, **7**, 3976-3984.
136. H.-X. Mai, Y.-W. Zhang, L.-D. Sun and C.-H. Yan, *The Journal of Physical Chemistry C*, 2007, **111**, 13721-13729.
137. W. Niu, S. Wu, S. Zhang and L. Li, *Chemical Communications*, 2010, **46**, 3908-3910.
138. A. M. Pires, S. Heer, H. U. Güdel and O. A. Serra, *Journal of fluorescence*, 2006, **16**, 461-468.
139. A. Punjabi, X. Wu, A. Tokatli-Apollon, M. El-Rifai, H. Lee, Y. Zhang, C. Wang, Z. Liu, E. M. Chan and C. Duan, *ACS nano*, 2014, **8**, 10621-10630.
140. Y. Li, J. Zhang, X. Zhang, Y. Luo, X. Ren, H. Zhao, X. Wang, L. Sun and C. Yan, *The Journal of Physical Chemistry C*, 2009, **113**, 4413-4418.
141. Y. Wang, L. Tu, J. Zhao, Y. Sun, X. Kong and H. Zhang, *The Journal of Physical Chemistry C*, 2009, **113**, 7164-7169.
142. G. Chen, H. Liu, G. Somesfalean, H. Liang and Z. Zhang, *Nanotechnology*, 2009, **20**, 385704.
143. D. Chen, L. Liu, P. Huang, M. Ding, J. Zhong and Z. Ji, *The journal of physical chemistry letters*, 2015, **6**, 2833-2840.
144. J. Wang, F. Wang, C. Wang, Z. Liu and X. Liu, *Angewandte Chemie International Edition*, 2011, **50**, 10369-10372.
145. G. Tian, Z. Gu, L. Zhou, W. Yin, X. Liu, L. Yan, S. Jin, W. Ren, G. Xing and S. Li, *Advanced Materials*, 2012, **24**, 1226-1231.
146. E. Song, S. Ye, T. Liu, P. Du, R. Si, X. Jing, S. Ding, M. Peng, Q. Zhang and L. Wondraczek, *Advanced Science*, 2015.
147. H. Dong, L.-D. Sun, Y.-F. Wang, J. Ke, R. Si, J.-W. Xiao, G.-M. Lyu, S. Shi and C.-H. Yan, *Journal of the American Chemical Society*, 2015.
148. H. Dong, L.-D. Sun and C.-H. Yan, *Chemical Society Reviews*, 2015, **44**, 1608-1634.
149. H. S. Mader, P. Kele, S. M. Saleh and O. S. Wolfbeis, *Current opinion in chemical biology*, 2010, **14**, 582-596.
150. Z. Song, Y. G. Anissimov, J. Zhao, A. V. Nechaev, A. Nadort, D. Jin, T. W. Prow, M. S. Roberts and A. V. Zvyagin, *Journal of biomedical optics*, 2013, **18**, 061215-061215.
151. J. Jin, Y.-J. Gu, C. W.-Y. Man, J. Cheng, Z. Xu, Y. Zhang, H. Wang, V. H.-Y. Lee, S. H. Cheng and W.-T. Wong, *ACS Nano*, 2011, **5**, 7838-7847.
152. S. Wu, G. Han, D. J. Milliron, S. Aloni, V. Altoe, D. V. Talapin, B. E. Cohen and P. J. Schuck, *Proceedings of the National Academy of Sciences*, 2009, **106**, 10917-10921.
153. P. K. Jain, K. S. Lee, I. H. El-Sayed and M. A. El-Sayed, *The Journal of Physical Chemistry B*, 2006, **110**, 7238-7248.
154. C.-h. Huang, L. McCaughan and D. M. Gill, *Lightwave Technology, Journal of*, 1994, **12**, 803-809.
155. C. Strohhöfer and A. Polman, *Optical Materials*, 2003, **21**, 705-712.
156. X. Xie, N. Gao, R. Deng, Q. Sun, Q.-H. Xu and X. Liu, *Journal of the American Chemical Society*, 2013, **135**, 12608-12611.

157. Y.-F. Wang, G.-Y. Liu, L.-D. Sun, J.-W. Xiao, J.-C. Zhou and C.-H. Yan, *ACS Nano*, 2013, **7**, 7200-7206.
158. G. Turri, H. P. Jenssen, F. Cornacchia, M. Tonelli and M. Bass, *JOSA B*, 2009, **26**, 2084-2088.
159. G. Chen, G. Somesfalean, Y. Liu, Z. Zhang, Q. Sun and F. Wang, *Physical Review B*, 2007, **75**, 195204.
160. T. Li, C. Guo and L. Li, *Optics express*, 2013, **21**, 18281-18289.
161. G. A. Crosby and J. N. Demas, *The Journal of Physical Chemistry*, 1971, **75**, 991-1024.
162. L. S. Rohwer and J. E. Martin, *Journal of luminescence*, 2005, **115**, 77-90.
163. K. Laqua, W. Melhuish and M. Zander, *Pure and Applied Chemistry*, 1988, **60**, 1449-1460.
164. V. Tikhomirov, G. Adamo, A. Nikolaenko, V. Rodriguez, P. Gredin, M. Mortier, N. Zheludev and V. Moshchalkov, *Optics express*, 2010, **18**, 8836-8846.
165. H. Liu, C. T. Xu, D. Lindgren, H. Xie, D. Thomas, C. Gundlach and S. Andersson-Engels, *Nanoscale*, 2013, **5**, 4770-4775.
166. Q. Liu, Y. Sun, T. Yang, W. Feng, C. Li and F. Li, *Journal of the American Chemical Society*, 2011, **133**, 17122-17125.
167. A. D. Ostrowski, E. M. Chan, D. J. Gargas, E. M. Katz, G. Han, P. J. Schuck, D. J. Milliron and B. E. Cohen, *ACS nano*, 2012, **6**, 2686-2692.
168. C. T. Xu, P. Svenmarker, H. Liu, X. Wu, M. E. Messing, L. R. Wallenberg and S. Andersson-Engels, *ACS nano*, 2012, **6**, 4788-4795.
169. P. Huang, W. Zheng, S. Zhou, D. Tu, Z. Chen, H. Zhu, R. Li, E. Ma, M. Huang and X. Chen, *Angewandte Chemie International Edition*, 2014, **53**, 1252-1257.
170. X. Li, R. Wang, F. Zhang and D. Zhao, *Nano letters*, 2014, **14**, 3634-3639.
171. F. C. van Veggel, C. Dong, N. J. Johnson and J. Pichaandi, *Nanoscale*, 2012, **4**, 7309-7321.
172. S. Han, R. Deng, X. Xie and X. Liu, *Angewandte Chemie International Edition*, 2014, **53**, 11702-11715.
173. J. Hao, Y. Zhang and X. Wei, *Angewandte Chemie International Edition*, 2011, **50**, 6876-6880.
174. M. D. Wisser, M. Chea, Y. Lin, D. M. Wu, W. L. Mao, A. Salleo and J. A. Dionne, *Nano letters*, 2015, **15**, 1891-1897.
175. G. Chen, H. Liu, H. Liang, G. Somesfalean and Z. Zhang, *The Journal of Physical Chemistry C*, 2008, **112**, 12030-12036.
176. C. Zhao, X. Kong, X. Liu, L. Tu, F. Wu, Y. Zhang, K. Liu, Q. Zeng and H. Zhang, *Nanoscale*, 2013, **5**, 8084-8089.
177. J. Tang, L. Chen, J. Li, Z. Wang, J. Zhang, L. Zhang, Y. Luo and X. Wang, *Nanoscale*, 2015, **7**, 14752-14759.
178. M. K. G. Jayakumar, K. Huang and Y. Zhang, *Nanoscale*, 2014, **6**, 8439-8440.
179. A. Yin, Y. Zhang, L. Sun and C. Yan, *Nanoscale*, 2010, **2**, 953-959.
180. H. Zhang, Y. Li, Y. Lin, Y. Huang and X. Duan, *Nanoscale*, 2011, **3**, 963-966.
181. J. Zhou, G. Chen, Y. Zhu, L. Huo, W. Mao, D. Zou, X. Sun, E. Wu, H. Zeng and J. Zhang, *Journal of Materials Chemistry C*, 2015, **3**, 364-369.
182. R. Arppe, I. Hyppänen, N. Perälä, R. Peltomaa, M. Kaiser, C. Würth, S. Christ, U. Resch-Genger, M. Schäferling and T. Soukka, *Nanoscale*, 2015, **7**, 11746-11757.
183. X. Chen, D. Peng, Q. Ju and F. Wang, *Chemical Society Reviews*, 2015, **44**, 1318-1330.
184. E. Hemmer, M. Quintanilla, F. Légaré and F. Vetrone, *Chemistry of Materials*, 2014, **27**, 235-244.
185. A. E. Guller, A. N. Generalova, E. V. Petersen, A. V. Nechaev, I. A. Trusova, N. N. Landyshev, A. Nadort, E. A. Grebenik, S. M. Deyev and A. B. Shekhter, *Nano Research*, 2015, **8**, 1546-1562.
186. G. Chen, H. Ågren, T. Y. Ohulchanskyy and P. N. Prasad, *Chemical Society Reviews*, 2015, **44**, 1680-1713.
187. D. Chen and P. Huang, *Dalton Trans.*, 2014, **43**, 11299-11304.

188. X. Huang, *Journal of Alloys and Compounds*, 2015, **628**, 240-244.
189. W. Shao, G. Chen, T. Y. Ohulchanskyy, A. Kuzmin, J. Damasco, H. Qiu, C. Yang, H. Ågren and P. N. Prasad, *Advanced Optical Materials*, 2015, **3**, 575-582.
190. E. M. Purcell, H. Torrey and R. V. Pound, *Physical review*, 1946, **69**, 37.
191. M. Saboktakin, X. Ye, S. J. Oh, S.-H. Hong, A. T. Fafarman, U. K. Chettiar, N. Engheta, C. B. Murray and C. R. Kagan, *ACS nano*, 2012, **6**, 8758-8766.
192. S. Schietinger, T. Aichele, H.-Q. Wang, T. Nann and O. Benson, *Nano letters*, 2009, **10**, 134-138.
193. D. Wei, L. Sudheendra, Z. Jiangbo, F. Junxiang, J. Dayong, M. K. Ian and M. G. Ewa, *Nanotechnology*, 2011, **22**, 325604.
194. S. Rohani, M. Quintanilla, S. Tuccio, F. De Angelis, E. Cantelar, A. O. Govorov, L. Razzari and F. Vetrone, *Advanced Optical Materials*, 2015.
195. J. Liao, Z. Yang, S. Lai, B. Shao, J. Li, J. Qiu, Z. Song and Y. Yang, *The Journal of Physical Chemistry C*, 2014, **118**, 17992-17999.
196. J. H. Lin, H. Y. Liou, C.-D. Wang, C.-Y. Tseng, C.-T. Lee, C.-C. Ting, H.-C. Kan and C. C. Hsu, *ACS Photonics*, 2015, **2**, 530-536.
197. A. Gnach, T. Lipinski, A. Bednarkiewicz, J. Rybka and J. A. Capobianco, *Chemical Society Reviews*, 2015, **44**, 1561-1584.
198. N. C. Mueller and B. Nowack, *Environmental science & technology*, 2008, **42**, 4447-4453.
199. Y. Lu, J. Zhao, R. Zhang, Y. Liu, D. Liu, E. M. Goldys, X. Yang, P. Xi, A. Sunna and J. Lu, *Nature Photonics*, 2014, **8**, 32-36.
200. F. Zhang, R. Che, X. Li, C. Yao, J. Yang, D. Shen, P. Hu, W. Li and D. Zhao, *Nano letters*, 2012, **12**, 2852-2858.